Gondwana Research 106 (2022) 142–163

Contents lists available at ScienceDirect

Gondwana Research

journal homepage: www.elsevier.com/locate/gr

Crustal structure and tectonic evolution of Greater Maldive Ridge, Western Indian Ocean, in the context of plume-ridge interaction

Priyesh Kunnummal, S.P. Anand *

Indian Institute of Geomagnetism, Navi Mumbai, Maharashtra 410218, India

ARTICLE INFO

Article history:
Received 20 May 2021
Revised 8 December 2021
Accepted 6 January 2022
Available online 11 January 2022
Handling Editor: A. Vasanthi

Keywords:
Plume-ridge interaction
Maldive ridge
Geoid to topography ratio
Effective elastic thickness
Satellite derived free-air gravity
Curie depth

ABSTRACT

The Greater Maldive Ridge (GMR), consisting of the Maldive Ridge (MR) and Deep Sea Channel (DSC) region, is the N-S trending, middle segment of Chagos-Laccadive Ridge system. This ridge system is widely considered to be the repository representing the interaction between Central Indian Ridge spreading centre and Reunion plume. The present study investigates in detail, spatial variations in effective elastic thickness (T_e), isostasy and crustal structure of GMR using high resolution satellite derived gravity, residual geoid and bathymetry data. Estimated T_e values along the GMR from 2D and 3D flexural modelling ranges from 6.5–16.5 km with comparatively lower T_e values over MR (7–9 km) and slightly higher values over the DSC region (>10 km). Geoid to Topography Ratio computed for two wavelength bands shows almost similar kind of variation along the ridge with a maximum value of 1.4 m/km in the DSC region, decreasing northwards to 0.6 m/km over MR. Integrating results from the present study with crustal thickness, Moho undulations and Curie depth along the entire length of the GMR suggest that MR was formed in the vicinity of spreading centre while DSC region was under a long transform fault which has given rise to the gap zone between Chagos Bank and Maldive Ridge during plume-ridge interaction.

1. Introduction

The northern Indian Ocean comprises number of aseismic ridges (Ninety East Ridge, Eighty Five East Ridge, Laxmi Ridge, Chagos-Laccadive Ridge, etc.) some of which protrude high above the ocean floor. These ridges are considered to be the repositories of several major tectonic processes including the northward motion of India during the opening of the Indian Ocean, lithospheric plate reorganizations, interactions between spreading centers and mantle plume or plate-plume interactions, and continental collisions. One such prominent aseismic ridge in the Western Indian Ocean is the approximately 3000 km long, north–south running, slightly arcuate shaped Chagos-Laccadive Ridge (CLR) located between latitudes 10°S and 15°N (Fig. 1). The CLR system consists of mainly three segments, the Laccadive Ridge (Lakshadweep) in the north, Maldive Ridge in the middle and Chagos Bank in the south (Bhattacharya and Chaubey, 2001). The nature of the crust underlying the CLR i.e., whether it is continental or oceanic, and its genesis is still controversial and several theories were put forth for its evolution (Kunnummal et al., 2018 and references therein). Among the several theories put forth for its evolution, the formation of the CLR due to the Reunion hotspot activity (Francis and Shor, 1966; Dietz and Holden (1970); Morgan, 1981) as the Indian plate moved over the hotspot gained wide popularity as few DSDP/ODP wells drilled over different segments of the ridge encountered basalts of younger age (~41 Ma to ~ 65 Ma) (Backman et al., 1988; Duncan and Hargraves, 1990). In this context, the interaction of Reunion hotspot with the Central Indian Ridge was proposed to be the possible genesis of the Maldive Ridge in the regional studies carried out over the Chagos-Laccadive Ridge (e.g., Tiwari et al., 2007; Bredow et al., 2017; Sreejith et al., 2019). However, the tectonic evolution suggested for the Maldive Ridge by these studies differ each other about the tectonic setting in which the ridge was emplaced; i.e., whether it was formed in the vicinity of ridge axis (Bredow et al., 2017), near to the spreading ridge (Ashalatha et al., 1991; Tiwari et al., 2007) and/or on the flanks of the CIR (Sreejith et al., 2019). Earlier studies have reported magmatic underplating associated with Reunion plume throughout the length of the CLR (Gupta et al., 2010; Fontaine et al., 2015). The crustal thickness estimated over the Greater Maldive Ridge (Maldive Ridge and Deep Sea channel) predicted a decrease in crustal thickness from 27 km below the Maldive Ridge to ~ 9 km in the DSC region (Kunnummal et al., 2018). Further, an eastward extension of fracture zones

* Corresponding author.
E-mail address: aerospl@yahoo.co.uk (S.P. Anand).

https://doi.org/10.1016/j.gr.2022.01.006
1342-937X/

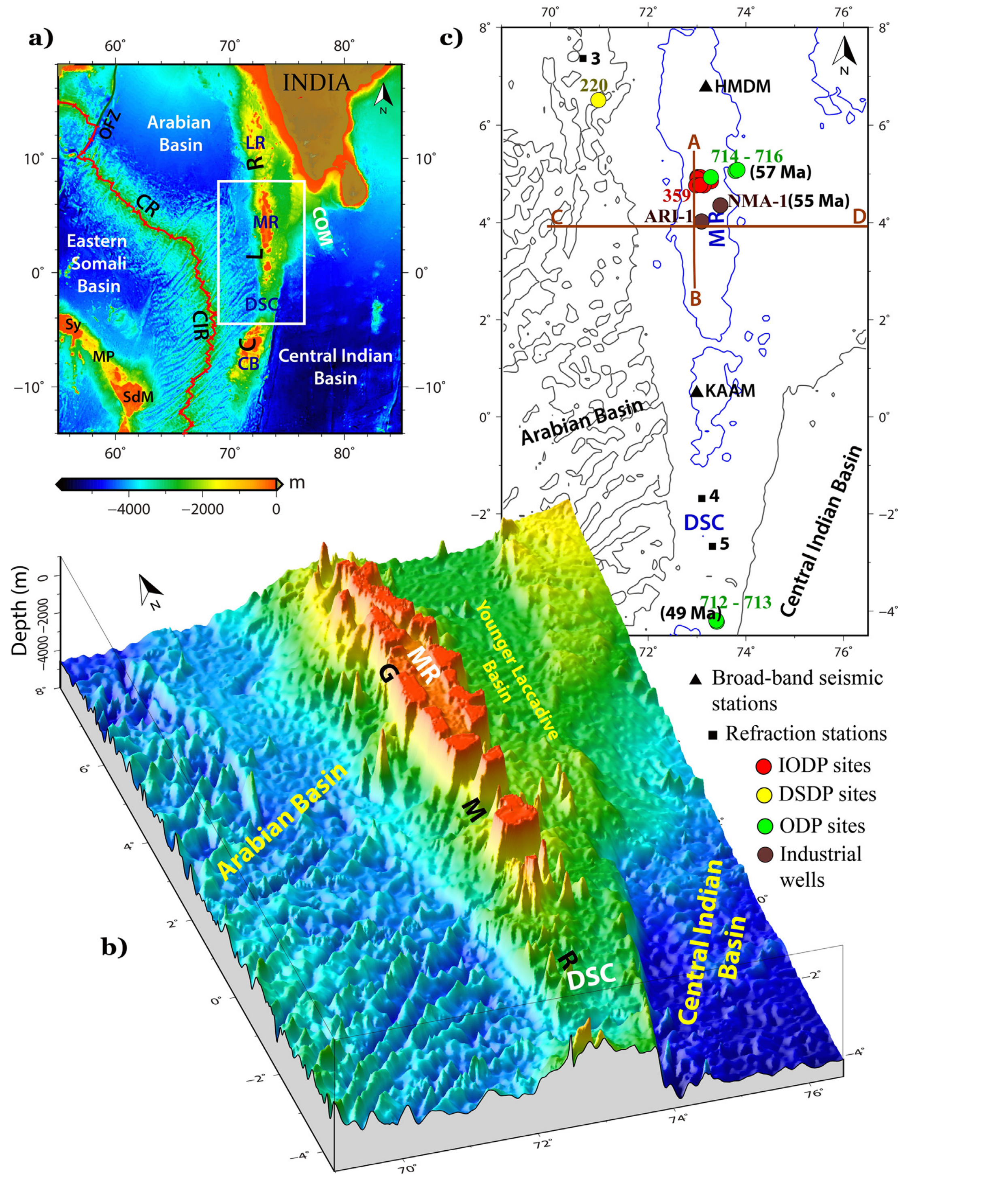

Fig. 1. a) Bathymetry map of the Western Indian Ocean generated from satellite altimetry (Smith and Sandwell, 1997) depicting the major structural features in the study region and adjacent areas. The study region is shown in white rectangular box. b) 3D bathymetry of the Greater Maldive Ridge. c) The solid black triangles and squares respectively indicates seismic refraction stations (Francis and Shor, 1966) and the location of permanent broadband seismic stations used for receiver function studies (Fontaine et al., 2015). The profile AB and CD respectively show the locations of profile used for modelling the crustal structure from FAG-IOGL data after Kunnummal and Anand (2019) (along AB) and in the present study (along CD). **MR**: Maldive Ridge, **DSC**: Deep Sea Channel, **GMR**: Greater Maldive Ridge, **CIR**: Central Indian Ridge, **CR**: Carlsberg Ridge, **CLR**: Chagos Laccadive Ridge, **LR**: Laccadive Ridge, **OFZ**: Owen Fracture Zone, **Sy**: Seychelles, **MP**: Mascarene Plateau, **SdM**: Saya de Malha, **COM**: Comorin Ridge.

(FZs) associated with spreading of Central Indian Ridge was found in the DSC region with an abrupt truncation at Vishnu Fracture Zone (Kunnummal and Anand, 2019), though no such FZs were identified over the Maldive Ridge. A better perspective of the crustal structure and tectonic evolution of Greater Maldive Ridge is needed to explain these observations.

The tectonic evolution of a seafloor bathymetric feature are primarily governed by the properties of the oceanic lithosphere. One, such parameter which is sensitive to the tectonic setting of the seafloor bathymetric feature is the effective elastic thickness (T_e), which can be used as a proxy for understanding the long-term strength of the lithosphere (Watts, 2001). The gravity and residual geoid data observed over the sea surface are sensitive to this parameter. Therefore, an investigation of flexure of the lithosphere in response to bathymetric loading, using bathymetry, gravity and residual geoid datasets helps to determine the T_e. An understanding of the spatial variation of T_e along the bathymetric feature provide vital information on the structure and tectonic evolution of the ridge and also provide clues about plume-ridge interaction i.e., whether the ridge is formed on, near, or far from a mid-ocean ridge when integrated with other proxies like crustal thickness, heat flow, etc. (Watts, 2001; Watts et al., 2006). An in depth understanding of the isostatic compensation mechanism and the variation of effective elastic thickness over each segment of the Chagos-Laccadive Ridge System (CLR) is essential in order to comprehend its tectonic evolution. Most of the previously estimated T_e values over the Chagos-Laccadive Ridge system were based on regional studies, (Ashalatha et al., 1991; Tiwari et al., 2007; Trivedi et al., 2012; Sreejith et al., 2019) while few other studies, e.g., Chaubey et al., (2008) attempted detailed investigation of isostasy of Laccadive segment of the CLR. However, so far no studies exclusively for understanding the isostasy and determination of effective elastic thickness over the Maldive Ridge and DSC region have been carried out. Among a number of geophysical studies dealing with the isostasy and determination of T_e in the nearby areas of the study region, it could be worth to mention here the studies by Radhakrishna (1996), Chand and Subrahmanyam (2003), Bansal et al., (2005), Dev et al., (2007), Ratheesh-Kumar et al., (2015), Ratheesh-Kumar and Xiao (2018) and Mishra et al., (2018, 2020). These studies mainly cover the T_e evaluation of Central Indian Ridge, Western Continental Margin of India, Owen transform fault and Laxmi Ridge. Therefore the present study investigates in detail, the spatial variations in effective elastic thickness and isostasy of Greater Maldive Ridge (GMR) using high resolution satellite derived gravity, residual geoid and bathymetry data to better understand its tectonic evolution. The main objectives of the present study are i) detailed analysis of 2D and 3D flexural modelling using bathymetry-gravity as well as bathymetry-geoid relationship to obtain finer variation of T_e along the GMR, ii) investigation of Geoid to Topography Ratio variations along the ridge to examine its isostatic compensation mechanism, iii) to derive the crustal structure of Maldive Ridge, iv) combine these information with previously published data of crustal thickness, Moho depth and Curie depth along the entire length of the GMR to understand how the Reunion-plume interaction with the Central Indian Ridge shaped its crustal structure pattern.

2. Morpho-tectonic elements and previous studies

The bathymetric map of the western Indian Ocean encompassing the study region and its major morphological and tectonic features are shown in Fig. 1. The study region includes the Maldive Ridge, the Deep Sea Channel region (i.e., the region between the Maldive Ridge and the Chagos Bank) (herein referred to as Greater Maldive Ridge – GMR) and the adjacent Arabian and Central Indian Basins. The Maldive Ridge extends for about 900 km between the latitudes 0.5°S and 7.5°N as a N-S trending bathymetric high feature. The ridge is bounded in the west by the seafloor of Arabian Basin and in the East by the Central Indian Basin. The ridge is overlain by an archipelago of coral islands grouped in a double row of atolls parted by an inner sea, which forms the Indian Ocean's most extensive coral reef and atoll community. Over the Maldive Ridge, eight IODP wells (expedition 359, Betzler et al., 2017), three ODP wells (leg 115, sites 714,715,716, Backman et al., 1988) and few industrial wells were drilled (location shown in Fig. 1). The ODP well 715 reached up to an olivine basaltic basement of Early Eocene age (57 Ma) about 211 m below seafloor (Backman et al., 1988) and it was suggested that at this site the lava solidified at sub-aerial depths (Duncan and Hargraves, 1990). Seismic reflection studies over the Maldive Ridge and the Maldive Inner Seas also suggested the presence of volcanic basement with sub-vertical faulting below the Eocene and Oligocene neritic carbonates (Aubert and Droxler, 1996; Belopolsky and Droxler, 2003; Betzler et al., 2017). The volcanic basement was subdivided into a 1 – 1.5 km thick lava flow unit (penetrated through drilling) followed by an acoustic basement (Aubert and Droxler, 1996) whose average depth to top was determined to be 5.5 km (Kunnummal and Anand, 2019) from satellite gravity data. Several studies have reported thicker crust and deepened Moho (>25 km) beneath the Maldive Ridge (e.g., Torsvik et al., 2013; Kunnummal et al., 2018). Receiver function modelling of broad-band seismic waveforms recorded at permanent seismic stations HMDM and KAAM located over the Maldive Ridge (location shown in Fig. 1) predicted a mean Moho depth of approximately 28 km and 23 km respectively beneath these stations (Fontaine et al., 2015). Further, seismic discontinuities in the shear wave velocity profile observed around 13 km over KAAM station and 14 km over HMDM stations (Fontaine et al., 2015) were inferred to represent the initial Moho interface before the underplating took place (presently top of the magmatic underplated rocks). The average depth to the top of the underplated material along the Maldive Ridge was found to be 11 km from the gravity study (Kunnummal and Anand, 2019). Oceanic spreading type anomalies were not identified along the CLR (Avraham and Bunce, 1977) whereas well-defined seafloor-spreading anomalies were identified in the Arabian Basin (Chaubey et al., 2002) and Central Indian Basin (McKenzie and Sclater, 1971; Cande et al., 2010; Cande and Patriat, 2015; Desa et al., 2019; Yatheesh et al., 2019).

The seismic refraction studies (Francis and Shor, 1966) in the Deep Sea Channel (region between Maldive Ridge and Chagos Bank) suggested that this region is underlain by a 1 km thick layer of 2.15 km/s velocity material at the top, followed by an about 4 to 5 km thick layer of probably volcanic material with a velocity of 6.13 km/sec. This region appears to interrupt the typically continuous hotspot trail between the Maldive Ridge and the Chagos Bank and suggested to be originated from a combination of ridge geometry, in particular the distribution of transform faults, plate motions and plume-ridge interaction (Bredow et al., 2017). Recently, integrating the results obtained from analysis of satellite gravity data along with seismic refraction studies (Francis and Shor, 1966), Kunnummal and Anand (2019) inferred that the crust below the DSC region is purely oceanic in nature.

3. Data sets used

In the present study, the most recent one arc-minute resolution global marine gravity model (Version 25.1, Sandwell and Smith, 2009; Sandwell et al., 2014) has been utilized. The main improvement of Version 25.1 with respect to Version 24.1 is the additional altimeter data from 12 months of CryoSat-2 LRM, 31 months of CryoSat-2 SAR and 13 months of data provided by the AltiKa altimeter onboard the SARAL spacecraft, launched in 2013 by the Indian Space Research Organization (ISRO) and French space agency, Centre National d'Etudes Spatiales (CNES). Version 25.1 of the free-air gravity data contain information down to very short wavelengths (<20 km) and hence can be employed for regional as well as detailed tectonic investigations. As the study region overlies the Indian Ocean Geoid Low (IOGL), (Kahle et al., 1978; Ghosh et al., 2017) the associated long wavelength gravity anomalies was computed using the spherical harmonic coefficient of EIGEN-6C4 geoid model (Förste et al., 2015) up to a degree and order of 50 (~800 km) (the coefficients are smoothly rolled off between the degrees 30–70) and removed from the Free-air gravity anomaly to obtain the FAG-IOGL map (Fig. 2a).

The main bathymetric dataset used is the latest one-arc minute resolution global seafloor topography (Version 18.1, Smith and Sandwell, 1997). A good coherency was shown between ship-borne bathymetry and bathymetry by Smith and Sandwell (1997) for wavelengths > 100 km which suggests that the later bathymetry data set can be utilized for studies related to crustal thickness and/or the elastic thickness of the lithosphere. Additionally the General Bathymetric Chart of the Oceans (GEBCO, 2021) with 15-arc second resolution obtained from British Oceanographic Data Centre (BODC) has also been used for the comparison of results. The residual geoid anomalies over the region were also utilized for computations. For this, the high resolution geoid data of the northern Indian Ocean was first generated using the latest available one arc-minute resolution global mean surface height (DTU15MSS) and mean dynamic topography (DTU15MDT) data sets of Andersen et al. (2019). The residual geoid anomalies (Sreejith et al., 2013) were then computed by removing the long wavelength geoid anomalies using the spherical harmonic coefficient of EIGEN- 6C4 (Förste et al., 2015) up to a degree and order of 50, the coefficients are rolled off smoothly between the degrees 30–70. Similarly, the residual topography data are prepared by removing the spherical harmonic expansion of model topography up to degree and order 50 (http://icgem.gfz-potsdam.de, Barthelmes and Köhler, 2016) from the bathymetric data. The residual geoid data generated here largely reflects the lithospheric-scale structures (this data is provided in the supporting information Fig. S1).

In addition to the above data sets, we have used results from ODP-IODP-DSDP wells, (Backman et al., 1988; Duncan and Hargraves, 1990; Betzler et al., 2017) and few industrial wells (Aubert and Droxler, 1996) available over the study region along with total sediment thickness grid of the world oceans, version 2 (Whittaker et al., 2013; Divins, 2003), where ever necessary. We have also utilized various published data sets over the Greater Maldive Ridge including the crustal thickness estimates from three-dimensional inversion of gravity anomalies by Kunnummal et al. (2018) and Curie depth mapped from the EMAG-2 magnetic data (Li et al., 2017).

4. Methodology and data analysis

4.1. Flexural modelling

The lithosphere can be modelled assuming it as a thin elastic plate overlying an inviscid fluid substratum that flexes elastically in response to vertical loads under the assumption that the plate

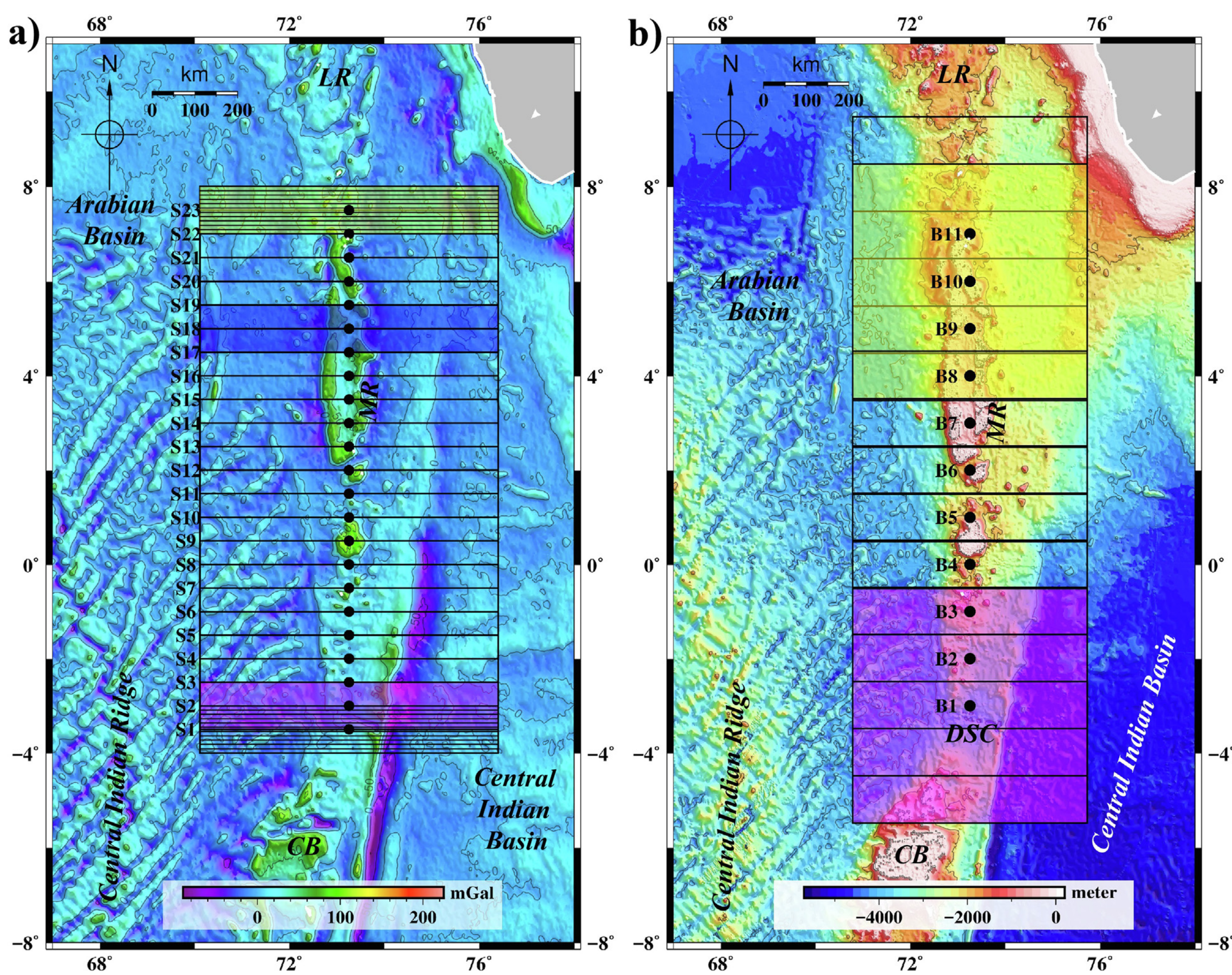

Fig. 2. a) FAG-IOGL gravity anomaly map over the Maldive Ridge and adjoining regions. The long wavelength gravity effect of Indian Ocean Geoidal Low (IOGL) is calculated using the spherical harmonic coefficient of EIGEN-6C4 (Förste et al., 2015) up to degree and order 50 and is removed from the FAG anomaly (V.25.1, Sandwell and Smith, 2009; Sandwell et al., 2014). Locations of median stacked profiles (S1 to S23) used for 2D flexural modelling is superposed. Median stacking has been done on profiles extracted with 10 km interval in a rectangular box of width 1° (110 km) and considering 0.5° overlap between each box. b) Bathymetry of the study region (GEBCO-2021). Locations of overlapping grids (B1 to B11) used for 3D flexural modelling are superposed. The grid size is taken as 550 km X 550 km with 1°overlap. **LR** = Laccadive Ridge; **MR**: Maldive Ridg; **DSC** = Deep Sea Channel region; **CB** = Chagos Bank.

thickness is small compared to the radii of plate curvature and the deflections are small related to plate thickness (Watts, 2001). Gravity and residual geoid anomalies are sensitive indicators of the flexural properties of the lithosphere. Combined with isostasy (Dorman and Lewis, 1970) and Fourier domain expressions of gravity anomalies (Parker, 1973), along with the thin elastic plate flexure model, the relationship between the topographic loads and the underlying Moho deflections as well as the gravity response to each can be written as the sum of a linear term (first term) and two nonlinear terms, (second term) and (third term): (Lyons et al., 2000)

$$G(k) = 2\pi G(\rho_l - \rho_w)e^{-2\pi|k|s}B(k)\left[1 - e^{-2\pi|k|d}R(|k|)\right] + 2\pi G(\rho_l - \rho_w)e^{-2\pi|k|s}\sum_{n=2}^{\infty}\left(\frac{|2\pi k|^{n-1}}{n!}F\{b^n(r)\}\right) + 2\pi G(\rho_m - \rho_c)e^{-2\pi|k|(s+d)}\sum_{n=2}^{\infty}\left(\frac{|2\pi k|^{n-1}}{n!}F\{m^n(r)\}\right). \quad (1)$$

where G represents the gravitational constant, s is the average depth of the area from the mean sea level, d is the average crustal thickness. $G(k)$ and $B(k)$ represents the Fourier transform of gravity and bathymetry respectively. F and F^{-1} represent the forward and inverse Fourier transform operations respectively. k denotes the wavenumber vector $\left(\frac{1}{\lambda}\right)$. The densities of the seawater, load, crust and mantle in kg/m^3 are represented by ρ_w, ρ_l, ρ_c and ρ_m respectively.

The first term on the right hand side of the expression (1) approximates the linear contribution of gravity anomalies from both the bathymetry of the ocean floor $b(r)$ and Moho undulations $m(r)$ while the second and third term provides the higher order effects of bathymetry and Moho topography respectively on the gravity anomalies. The Moho undulations $m(r)$ are expressed using thin elastic plate flexure model, as

$$m(r) = F^{-1}\left\{-\left(\frac{\rho_l - \rho_w}{\rho_m - \rho_c}\right)R(|k|)B(k)\right\}, \quad (2)$$

with $R(|k|)$, being the wavenumber parameter that modifies the Airy response to produce the flexural response and is given by

$$R(|k|) = \left(1 + \frac{D|2\pi k|^4}{g(\rho_m - \rho_c)}\right)^{-1}. \quad (3)$$

where, g is the mean acceleration due to gravity. The relationship connecting the flexural rigidity (D) to the effective elastic thickness (T_e) is given by

$$D = \frac{ET_e^3}{12(1 - \vartheta^2)}. \quad (4)$$

where, E is the Young's modulus and ϑ is the Poisson's ratio (Watts, 2001).

Similarly, the geoid response is readily obtained from the equation: (e.g., Chapman, 1979).

$$G_{geoid}(k) = \frac{G(k)}{g * 2\pi|k|}. \quad (5)$$

Flexural modelling involves, the use of expression (1) and (5) to calculate the gravity and geoid effect of regionally compensated bathymetry for various values of elastic thickness (T_e) by assuming the values of crustal thickness and densities of load, crust and mantle. The computed gravity or geoid anomalies are compared with the observed anomalies and the best fitting value of T_e is selected based on minimum misfit criterion. In the present study, the best fitting T_e is considered based on the minimum objective function criteria (Eq. (6)) instead of simple RMS misfit in order to achieve a good discrimination of T_e (Smith et al., 1989). The objective function can be expressed as,

$$Obj.fun. = 0.5 * \left[\frac{RMS}{RMS_{max}} + abs(Corr.Coeff.)\right]. \quad (6)$$

where, RMS_{max} represents the maximum RMS from the models of all T_e values, and is used to normalize the RMS range from 0 to 1. The absolute value of correlation coefficient between residual anomaly (i.e., the difference in observed and modelled gravity/geoid) and the bathymetry is used to confine the values of objective function within 0 and 1.

Most of the flexural studies carried out over the major aseismic ridges in the Indian Ocean considered only the first order theory and ignored the gravity effects originating from higher order terms of seafloor topography and its compensation (e.g., Paul and Singh, 1992; Sreejith and Krishna, 2013; Sreejith et al., 2019). Even though the linear approximation is adequate to describe the flexure due to the seamounts, as the first term in expression (1) contribute 90% of the total gravity anomaly, a number of studies have pointed out, the omission of nonlinear terms may significantly underestimate the gravity anomalies (Ribe, 1982; Lyons et al., 2000; Watts et al., 2006; Marks and Smith, 2007). The importance of inclusion of non-linear terms when modelling the gravity and geoid anomalies due to topographic load and its compensation is demonstrated in this paper using synthetic data and results. This exercise is provided in the appendix (Fig. 11 and Fig. 12). Another important aspect noted in the flexural modelling studies is the effect of assumption of two dimensionality for a three dimensional feature (Ribe, 1982; Filmer et al., 1993; Lyons et al., 2000) when modelling the gravity and geoid anomalies over profiles. Assumption of two dimensionality for a seamount introduces marked effects on the gravity anomalies and have large effect on T_e determination in flexural studies (Lyons et al., 2000). However, in the case of a line ridge, as demonstrated in the appendix of this paper (Fig. 12), the assumption of two dimensionality has little effect on the gravity and geoid anomalies.

In the present study, the flexural modelling has been carried out using both bathymetry-gravity as well as bathymetry-geoid relationship, along the Greater Maldive Ridge to infer the spatial variations in effective elastic thickness (T_e), a proxy governing the integral strength of the lithosphere. For the computation of the effective elastic thickness (T_e), we have used Indian Ocean geoidal low removed Free-air gravity data (FAG-IOGL), residual geoid and the residual bathymetry. To check the changes in T_e, if any, introduced as a result of removing the IOGL, we have computed T_e using Free-air gravity data as well. The result of this exercise is shown in Table S1 in the supplementary section. As the T_e values are highly dependent on the bathymetry of the region, present study utilized bathymetric data derived by Smith and Sandwell (1997) from satellite altimetric measurements and General Bathymetric Chart of Ocean (GEBCO, 2021) computed from depth soundings, for comparison.

The higher order terms of both bathymetry and Moho topography are evaluated up to the order n = 5. A mean and linear trend was removed from the data which was further extended and tapered using a Hanning window prior to the Fourier domain computations. Ten percentage of the gravity/geoid data from the borders were not considered during the comparison of observed and modelled anomalies with a view to avoid edge effects. The upper and lower limits of T_e are defined by points of intersection where the objective function minima has increased by 10% of the assigned objective function. The parameters used for the flexural modelling are listed in Table 1. A density of 2550 kg/m^3 is considered for the load of the ridge, which is the average density of the carbonate

Table 1
Model parameters used for 2D and 3D flexural modelling.

Parameter	Value
Universal gravitational constant ($\boldsymbol{G}$)	6.67 $m^3kg^{-1}s^{-2}$
Acceleration due to gravity ($\boldsymbol{g}$)	9.806 ms^{-2}
Young's modulus ($\boldsymbol{E}$)	100 GPa
Poison ratio (ϑ)	0.25
Seawater density ($\boldsymbol{\rho_w}$)	1030 kg/m^3
Density of load ($\boldsymbol{\rho_l}$)	2550 kg/m^3
Density of crust ($\boldsymbol{\rho_c}$)	2900 kg/m^3
Density of Mantle ($\boldsymbol{\rho_m}$)	3300 kg/m^3
Average crustal thickness ($\boldsymbol{d}$)	7 km

platform (2300 kg/m^3) and the lava flow unit (2800 kg/m^3). The average depth to the top of the load is assumed to be 5.5 km, which is the mean depth to the top of the acoustic basement obtained from the analysis of radially averaged power spectrum, the gravity modelling (Kunnummal and Anand, 2019) and seismic reflection profiles (Aubert and Droxler, 1996). The computations were performed for both 2D (along profiles) and 3D (grids) cases.

As demonstrated in the appendix, the 2D flexural modelling over the profiles extracted perpendicular to the linear ridge axis with sufficient profile length, provides reliable T_e estimates and helps to obtain finer T_e variations. The Maldive Ridge can be considered as a linear ridge, having a width>100 km. Therefore in the present study, in order to obtain finer variations in T_e, the two dimensional flexural modelling has been carried out using number of closely spaced profiles as well as median stacked profiles along the Maldive Ridge and Deep Sea Channel region. For the safe assumption of two dimensionality the residual bathymetry, residual geoid and the FAG-IOGL gravity data along the profiles were extracted perpendicular to the ridge axis. A total of 23 profiles, each having a length of 600 km and a line spacing of 0.5° (~55 km) between each of them were used for modelling initially (refer Fig. 2a for profile locations). Considering the rugged topography along the Maldive Ridge and DSC region, same number of median stacked profiles were also prepared and used for analysis. Median stacking has been done on profiles extracted with 10 km interval in a rectangular box of width 1° (110 km) and considering 0.5° overlap between each box as shown in Fig. 2a. A representative plot of median stacked profile of residual bathymetry, residual geoid and FAG-IOGL gravity data together with a shaded envelope showing the upper and lower values encountered during the stacking is presented in the supporting information, Fig. S2. In order to check if the assumption of two dimensionality is introducing any variations in the T_e values calculated from the 2D flexural modelling (refer appendix for detailed discussion), three-dimensional flexural modelling has also been undertaken using the gridded residual bathymetry, FAG-IOGL gravity and residual geoid in 11 overlapping blocks along the Maldive Ridge and DSC region. The size of each block is selected as 550 km × 550 km with 1° overlap and the recovered T_e is assigned to the centre latitude of the grid. The location of these overlapping blocks, from south to north, are shown in Fig. 2b.

4.2. Geoid to topography Ratio (GTR) computation and analysis over GMR

For understanding the isostatic compensation mechanism of oceanic plateaus, swells and ridges, number of studies have examined the linear relationship between the residual geoid heights and topography for wavelengths larger than the flexural wavelength of the lithosphere (>330 km) (e.g., Sandwell and Renkin, 1988; Sandwell and Mackenzie, 1989; Monnereau and Cazenave, 1988; Luis and Neves, 2006; Tiwari et al., 2007; Rajesh and Majumdar, 2009; Sreejith and Krishna, 2013; Rao et al., 2016). Longer wavelength (>4000 km) components of geoid and topographies generally reflects the large scale effect of mantle dynamics, while in the waveband 330 km – 4000 km, the topographies are largely compensated and known to exhibit a linear relationship with geoid heights (e.g., Sandwell and Mackenzie, 1989). Implementation of bandpass filters to truncate the wavelengths outside the waveband (330 km – 4000 km) enables one to analyze the Geoid to Topography Ratios (GTR) in the space domain. Here, generally, a regression analysis using least square method is carried out on the residual geoid data plotted against the residual topography to obtain the slope (GTR) of the straight line fit. The bandlimited space domain analysis for determining geoid to topography ratio have the advantages that, it can be carried out on the geographic data itself and the areas can be selected using polygons defining the boundary of feature of interest, to avoid contaminating signals from the adjacent known geologically distinct features (Sandwell and Mackenzie, 1989). Studies have established that GTR ranging between, (**0–2**) m/km (low) corresponds to shallow Airy compensation with crustal thickening; (**2–6**) m/km (intermediate) corresponds to deeper levels of compensation by lithosphere thinning (Crough, 1978) or thermal isostasy / dynamic uplift from a mantle plume (Sandwell and Renkin, 1988); (**>6**) m/km (high) provides compensation below the lithosphere through convective stresses (McKenzie et al., 1980). The GTR values can be used to calculate apparent compensation depth (dc) using the Pratt's relation, (Monnereau and Cazenave, 1988; Rajesh and Majumdar, 2009; Sreejith and Krishna, 2013),

$$dc = \frac{g(GTR)}{\pi G(\rho_m - \rho_w)} \tag{7}$$

where, g is the mean acceleration due to gravity and G is the universal gravitational constant. ρ_w and ρ_m are the densities of water (1030 kg/m^3) and mantle (3300 kg/m^3) respectively.

In the present study GTR values over the Greater Maldive Ridge are computed using the residual geoid heights and residual topography prepared for two different wavelength bands. One wavelength band corresponds to 330 km to 2420 km and the other one to 330 km to 800 km. The two wavelength bands are considered to understand the sensitivity of the results with the cut off wavelength of the high pass filters. To bandpass filter the observed geoid and bathymetry data, the longer wavelength components reflecting the large scale effect of mantle dynamics are removed by subtracting anomalies corresponding to a low degree and order spherical harmonic coefficients while the shorter wavelength components associated with the lithospheric flexure were removed using a low pass Gaussian filter. The wavelength band 330 km – 2420 km are prepared by first removing a low degree and order spherical harmonic coefficients with gentle cut off from 8 (~5000 km) to 25 (~1600 km) from the observed geoid and bathymetry data, followed by applying a low pass Gaussian filter with a cut off wavelength of 330 km to remove the wavelengths <330 km. The bandpass filtered (330 km – 2420 km) maps of the geoid and bathymetry thus obtained are shown in Fig. 3. Similarly, to limit the geoid and topography anomalies with in the wavelength band 330 km – 800 km, (Fig. S3 in the supporting information) spherical harmonic coefficients of degree and order up to 50 (~800 km, cosine tapered between the degrees 30 to 70) were considered for high pass filtering. Using these bandpass filtered geoid and bathymetry data sets, Geoid to Topographic Ratio (GTR) was computed over GMR to infer the isostatic compensation mechanism of the ridge. The analysis are completed with and without the removal of isostatic effects of sediment load from the bathymetry (Sykes, 1996). The bandpass filtered bathymetry corrected for the isostatic effects of sediment load are shown in Fig. 3c; and

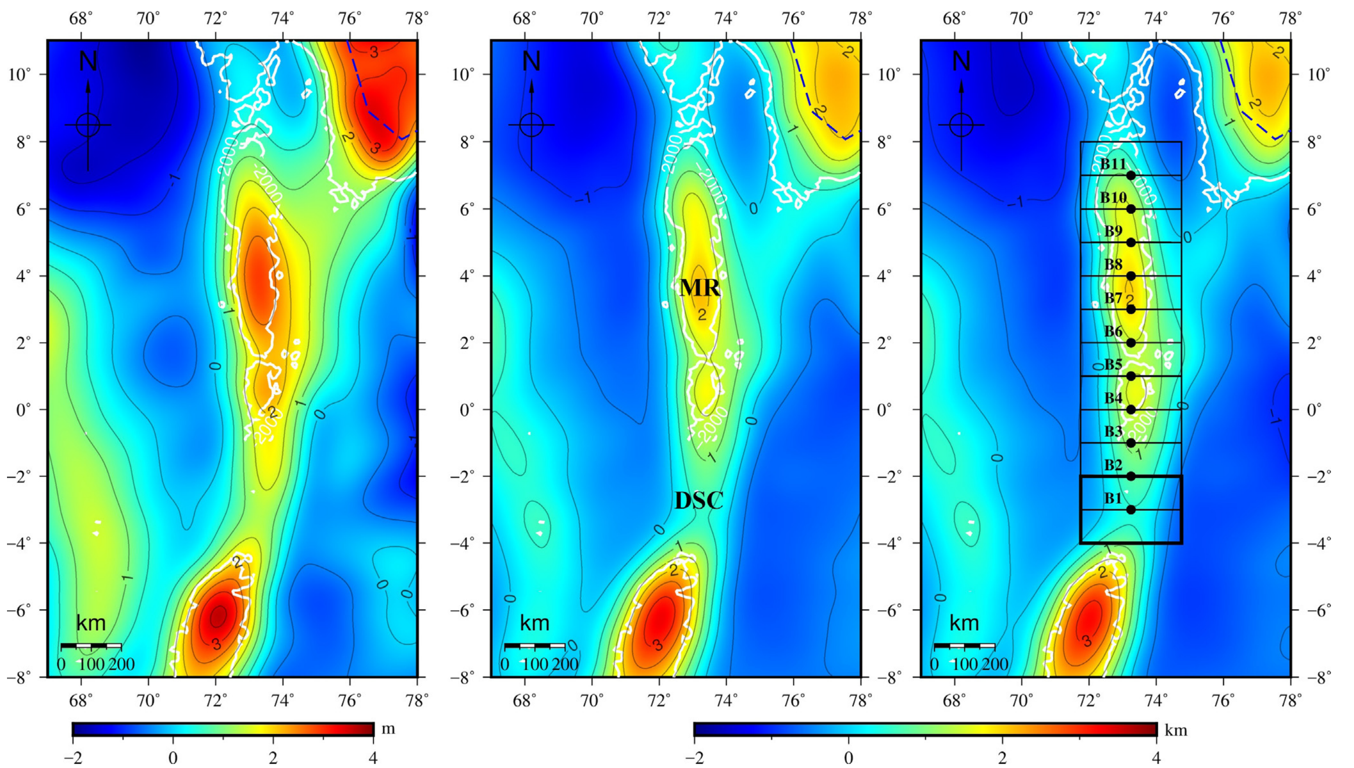

Fig. 3. Bandpass filtered geoid and bathymetry (330 km-2420 km). a) Bandpass filtered geoid. b) Bandpass filtered bathymetry. c) Bandpass filtered bathymetry corrected for isostatic effects of sediment load (Sykes, 1996). Black rectangular boxes represent the overlapping windows used for GTR analysis along the Maldive Ridge. 2000 m isobaths are superposed as white contour line. Dashed blue line represents crude resolution coastline. **MR**: Maldive Ridge; **DSC**: Deep Sea Channel. (For interpretation of the references to colour in this figure legend, the reader is referred to the web version of this article.)

Fig. S3c (in supporting information) respectively for the wavelength band 330 km – 2420 km and 330 km – 800 km. The highs and lows observed on the bandpass filtered geoid heights correlates well with that from filtered topography. Along with estimating the GTR values, the correlation coefficient which signifies the best fit are also estimated. The GTR values are converted into apparent depth of compensation using Eq. (7). In order to understand the spatial variations in GTR over the entire length of the Greater Maldive Ridge (GMR, i.e., MR plus DSC region) several overlapping blocks of size, 3°×2° with 1° overlap have been selected along the GMR (Fig. 3c) and GTR values were computed.

4.3. Modelling of the crustal structure along an E-W profile (CD) over Maldive Ridge

In order to derive the crustal structure across the Maldive Ridge two-dimensional forward modelling of Indian Ocean Geoidal Low corrected free-air gravity data has been undertaken along an E-W profile. This east–west profile (Profile CD in Fig. 1c) runs ~ 750 km from the Arabian Basin in the west, through Maldive Ridge and the Central Indian Basin in the east and intersects the two N-S seismic transects of Aubert and Droxler (1996) and also the N-S profile (Profile AB in Fig. 1c) modelled by Kunnummal and Anand (2019). The two industrial wells ARI-1 and NMA-1, slightly north of the profile, has been projected into this profile to constrain the initial depths to different layers. The 2D forward modelling was undertaken using the interactive GM-SYS profile modelling software (Geosoft, 2014). The computation of gravity anomalies is based on the method of Talwani et al. (1959) and makes use of the algorithms described in Won and Bevis (1987). Analogous to the previous crustal model (Kunnummal and Anand, 2019) derived along the N-S profile AB, a multi-layered crustal model is assumed for calculating the gravity response. Starting with bathymetry from the top, the layering follows the carbonate platform, lava flow unit, acoustic basement, underplated material and finally the mantle. The depth to the shallow layers were constrained utilizing the information from ARI-1, NMA-1 wells and from the two N-S seismic transects (Aubert and Droxler, 1996) at the location where the profile intersects the seismic transects. The starting depth to the top of acoustic basement and underplated material were taken from the depths obtained from the radially averaged power spectrum (after Kunnummal and Anand, 2019); while a starting model of variations in the Moho depth along the profile is assumed from the Moho predicted from the inversion of Mantle Residual Gravity anomalies from our earlier study Kunnummal et al. (2018). Carbonates on the top of the Maldive Ridge ranging in age from Paleogene to present was assumed an average density of 2.3 gm/cc whereas the lava flows was assigned an average density of 2.8 gm/cc (Backman et al., 1988). The acoustic basement, underplated material and the Mantle were respectively provided densities of 2.95 gm/cc, 3.05 gm/cc and 3.30 gm/cc. A density of 2.35 gm/cc is assumed for the sediments in the adjacent Arabian and Central Indian Basins. The gravity response of the model was computed and compared with the observed anomalies and then the model depths were adjusted iteratively in a way that best reproduces the observed gravity anomalies. In the present model, we have considered a density of 2.95 gm/cc for the entire crustal layer underlying Arabian Basin, MR and Central Indian Basin. However, a reworked continental crust (Kunnummal et al., 2018) with a density different from the assumed density cannot be ruled out for the Central Indian Basin region east of the Vishnu Fracture Zone. The final crustal structure derived across the Maldive Ridge is shown in Fig. 8.

5. Results

5.1. Flexural modelling

The results of the flexural modelling carried out over the single profiles and stacked profiles suggests that, in general, the T_e values obtained by 2D flexural modelling of bathymetry-gravity and bathymetry-geoid are more consistent when using the stacked profiles rather than for single profiles (See supporting information Fig. S4, a representative plot for comparison). This is true while using both, Smith & Sandwell and GEBCO-2021 bathymetry data. Accordingly, only the results from the modelling of stacked profiles are tabulated (Table 2). The observed gravity/geoid and the same predicted for the best fitting T_e, along with the bathymetry and objective response function misfit curves are shown in Fig. 4, from south to north, for few selected median stacked profiles (S2, S6, S13, S18). These are presented for both the Smith & Sandwell bathymetry and GEBCO-2021 bathymetry. The representative profiles S2 and S6 are located in the DSC region while S13 and S18 are over the Maldive Ridge (Fig. 2a). The average T_e obtained for the profiles S2 and S6 in the DSC region are about 14 km, while that deduced from the profiles S13 and S18 over the MR are 8.7 km. The flexural modelling results other than that shown in Fig. 4 are provided in the supplementary section (Fig. S6 to Fig. S15).

It can be seen that the T_e values inferred from the Smith & Sandwell bathymetry and GEBCO-2021 bathymetry are more or less identical (Table 2), there being no difference in many profiles and an average difference of 0.5 km along few profiles. However, the difference is 1 km in profiles S10 and S22, 1.5 km in S11 and 2 km in S12. This difference may be due to the fact that the bathymetry is changing rapidly across the region where these profiles are located and that the stacked profile is providing an average bathymetry along these profiles. The resulting unsteadiness in T_e values might be caused by the higher sensitivity of free-air gravity with the irregularity of the topography. Nevertheless, the trend of the data remains unaltered. In addition there is large difference in T_e computed from gravity and geoid data along these profiles (S10, S11, S12, S22). Interestingly, the T_e values deduced from all the median stacked profiles, from south to north along the GMR predicts comparatively higher values of T_e over DSC region (11 km – 16.5 km, from profiles S1 to S9), and lower values over the Maldive Ridge (6 km – 10 km, from profiles S10 to S23).

The T_e values determined using 3D flexural modelling from the overlapping blocks (B1 to B11, Fig. 2b) using FAG-IOGL gravity and residual geoid data for the two bathymetric datasets are summarized in the Table 3 along with the upper and lower limits of T_e values. The results of the flexural modelling of two representative blocks, B3 in the DSC region and B10 over the MR are provided in the Fig. 5 for both the Smith & Sandwell bathymetry and GEBCO-2021 bathymetry (results of remaining blocks are provided in the supplementary section, Fig. S16 to Fig. S24). The predicted T_e value from the blocks B3 and B10 are 12 km and 8 km respectively. It is notable that, the T_e values evaluated from the gravity and geoid are very close to each other and follow the same trend of variation along the GMR for both bathymetric datasets. As seen from 2D modelling, in 3D case also relatively higher T_e values are found over DSC region from the blocks B1 to B4 ($\geq$11 km), compared to values obtained over the Maldive Ridge, from the blocks B5 to B11 (<10 km). By and large, the spatial variation in T_e along the Greater Maldive Ridge computed from the 3D flexural modelling are comparable to that determined from the 2D flexural modelling both in magnitude and trend. The minor deviations in magnitude could be the result of averaging effect of the discrete windows selected. Since the profiles and discrete windows selected for the analysis extends to the adjacent basins, the obtained T_e value could reflect an average value for the segments analyzed. However, the results from the 2D flexural modelling reveal finer variations in T_e along the GMR at 55 km interval whereas the results from 3D modelling display the average T_e value at every 110 km along the GMR.

Table 2
Result of 2-dimensional flexural modelling using stacked profiles. See Fig. 2a for profile locations. The upper and lower bounds of T_e values are determined from the intersection of a line obtained by increasing the minima of objective function by 10% of the function on the misfit curve.

Profile No.	Centre Latitude (degree)	Effective elastic thickness, T_e (km)											
		Using Smith & Sandwell bathymetry data						Using GEBCO-2021 bathymetry data					
		FAG-IOGL – Residual Bathymetry			Residual Geoid - Residual Bathymetry			FAG-IOGL - Residual Bathymetry			Residual Geoid - Residual Bathymetry		
		Lower	Best fit	Upper	Lower	Best fit	Upper	Lower	Best fit	Upper	Lower	Best fit	Upper
S1	*−3.5*	14.7	**16.5**	18.2	14.8	**16**	16.9	15.1	**17**	19.2	15.7	**16.5**	17.3
S2	*−3*	12.7	**14.5**	16	14.3	**15**	16	12.9	**14.5**	16.3	14.4	**15.5**	16.1
S3	*−2.5*	11.4	**13**	14.2	12.8	**13.5**	14.6	11.3	**13**	14.2	12.8	**13.5**	14.6
S4	*−2*	12.8	**14.5**	16.1	13.5	**14.5**	15.6	12.8	**14.5**	16.4	13.6	**14.5**	15.7
S5	*−1.5*	13.6	**15.5**	17.2	13.7	**15**	15.9	13.2	**15**	17.1	13.6	**14.5**	15.5
S6	*−1*	11.5	**13.5**	15.1	13	**14**	14.8	11.3	**13**	14.6	12.7	**13.5**	14.5
S7	*−0.5*	10.6	**12**	13.4	12.6	**13.5**	14.3	10	**11.5**	13	12.1	**13**	14
S8	*0*	8.7	**10.5**	11.9	11.2	**12**	13	9	**11**	12.4	11.7	**12.5**	13.4
S9	*0.5*	9.4	**11**	12.8	9.5	**11**	11.9	9.9	**11.5**	12.9	10	**11**	12
S10	*1*	3.9	**7.5**	9.4	10.2	**11.5**	13	5.4	**8.5**	10.5	11.2	**12.5**	13.9
S11	*1.5*	0	**2.5**	5.5	10.3	**12**	13.4	0	**4**	6.4	10.9	**12.5**	14.3
S12	*2*	0	**3.5**	5.7	9.7	**11**	12.3	3.4	**5.5**	7	11.1	**12.5**	13.7
S13	*2.5*	7.5	**8.5**	9.6	8.5	**10**	11	7.1	**8.5**	9.5	8.9	**10**	11.1
S14	*3*	8.6	**10**	11	8.7	**9.5**	10.8	8.3	**9.5**	10.8	8.6	**9.5**	10.7
S15	*3.5*	7.6	**9**	10	8.3	**9.5**	10.3	7.4	**8.5**	9.6	8.4	**9.5**	10.2
S16	*4*	8.6	**9.5**	10.4	8.3	**9**	9.9	8.3	**9.5**	10.4	8.3	**9**	9.9
S17	*4.5*	7.8	**9**	9.8	8.4	**9.5**	10.2	8.1	**9**	9.8	8.6	**9.5**	10.2
S18	*5*	6.8	**7.5**	8.5	7.8	**8.5**	8.9	6.9	**8**	8.7	8.1	**8.5**	9.2
S19	*5.5*	7.1	**8**	8.9	7.7	**8.5**	8.9	7	**8**	8.8	7.6	**8**	8.8
S20	*6*	6.7	**8**	9.4	6.4	**7**	7.9	6.7	**8**	9	6.4	**7**	7.9
S21	*6.5*	7.9	**9**	10.2	6.9	**7.5**	7.8	7.4	**8.5**	9.8	6.6	**7.5**	7.9
S22	*7*	3.1	**5**	6.4	6.2	**7**	7.4	4.4	**6**	7	6.7	**7.5**	7.9
S23	*7.5*	0	**4**	6.1	8.3	**9**	9.4	0	**3.5**	6	8.2	**9**	9.5

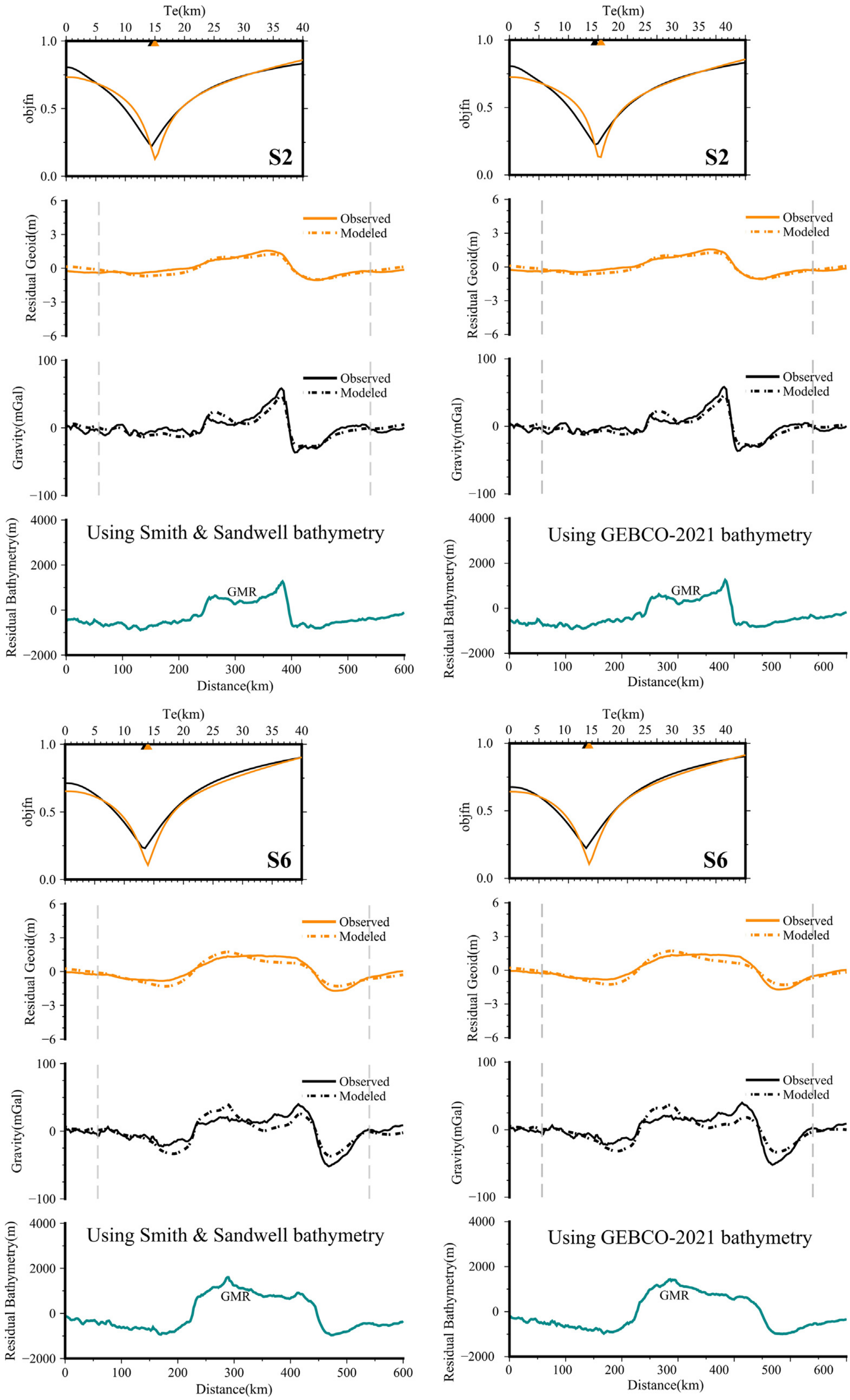

Fig. 4. Results of the 2D flexural modelling along the median stacked profiles S2 and S6 (DSC region) and S13 and S18 (Over Maldive Ridge). Orange coloured curves corresponds to geoid while black corresponds to FAG-IOGL gravity. (For interpretation of the references to colour in this figure legend, the reader is referred to the web version of this article.)

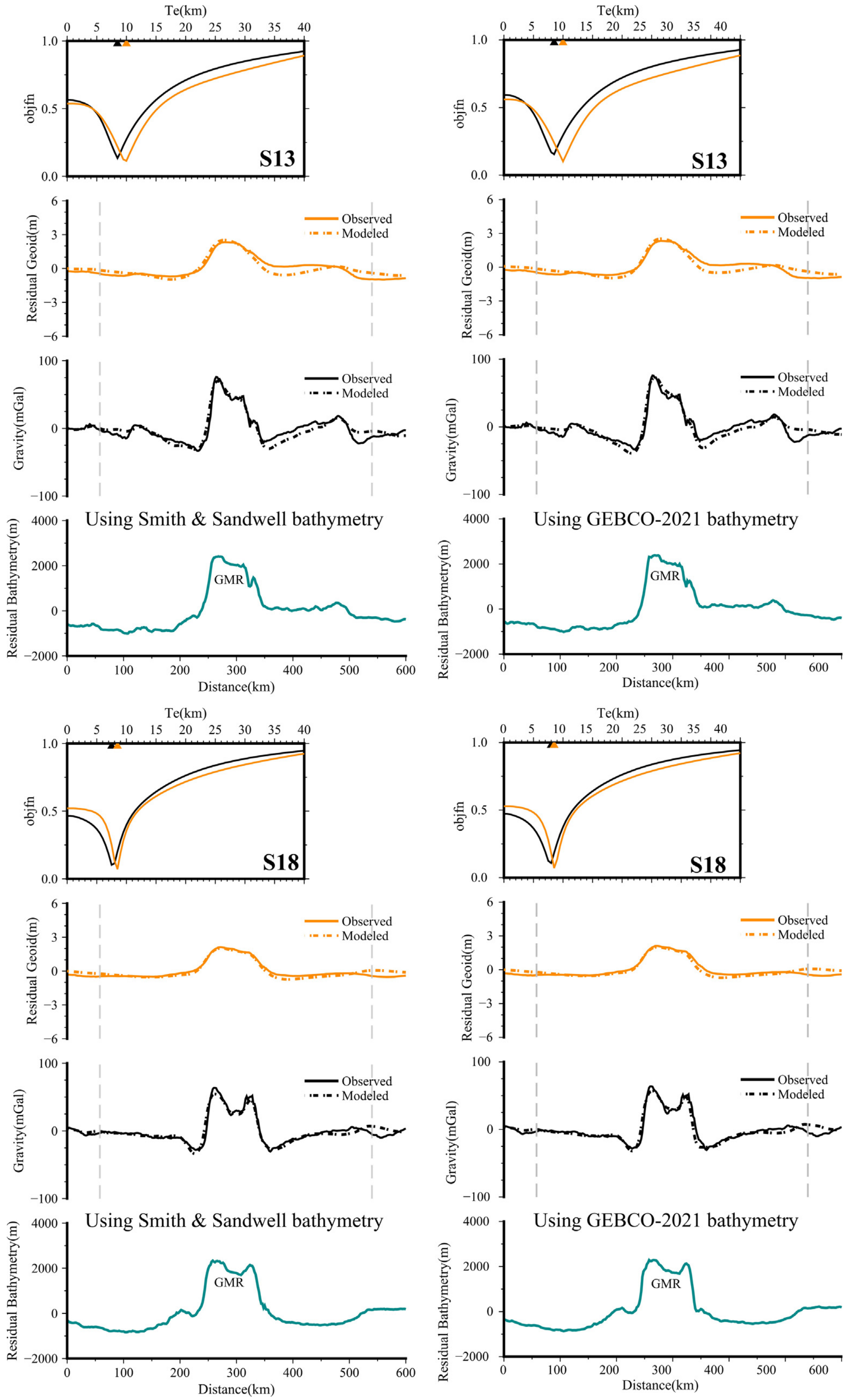

Fig. 4 (*continued*)

Table 3
Result of three dimensional flexural modelling carried out over 11 overlapping blocks along the Greater Maldive Ridge, from south to north. Refer Fig. 2b for the location of the blocks.

BlockNo.	Centre Latitude(degree)	Effective elastic thickness, T_e (km)											
		Using Smith & Sandwell bathymetry data						Using GEBCO-2021 bathymetry data					
		FAG-IOGL – Residual Bathymetry			Residual Geoid - Residual Bathymetry			FAG-IOGL – Residual Bathymetry			Residual Geoid - Residual Bathymetry		
		Lower	Best fit	Upper	Lower	Best fit	Upper	Lower	Best fit	Upper	Lower	Best fit	Upper
B1	*−3*	11.2	**13**	14.7	11.9	**13**	14	11.1	**13**	14.9	12	**13**	14.3
B2	*−2*	11.9	**14**	15.8	12.5	**13.5**	14.9	11.5	**13.5**	15.9	12.5	**13.5**	14.7
B3	*−1*	9.9	**11.5**	13.4	11	**12**	13.2	9.9	**12**	13.7	11.1	**12.5**	13.4
B4	*0*	9.4	**11.5**	13.2	10.7	**12**	13	9.7	**11.5**	13.6	11	**12**	13.1
B5	*1*	8.2	**10**	11.5	9.5	**10.5**	11.9	8.3	**10**	11.9	9.9	**11**	12
B6	*2*	7.3	**9**	10.3	8.6	**9.5**	10.4	7.6	**9**	10.5	8.7	**10**	10.9
B7	*3*	7.4	**9**	10.2	8.2	**9**	10.3	7.6	**9**	10.1	8.4	**9.5**	10.3
B8	*4*	7.3	**8.5**	9.9	7.9	**9**	9.7	7.4	**8.5**	9.7	8	**9**	9.6
B9	*5*	7	**8.5**	9.6	7.3	**8**	9.1	6.8	**8.5**	9.6	7.3	**8.5**	9.1
B10	*6*	6.6	**8**	9.6	7.3	**8**	8.9	6.6	**8**	9.5	7.3	**8**	9
B11	*7*	6.3	**8**	9.5	7.1	**8**	8.9	6.4	**8**	9.4	7.1	**8**	9

5.2. Geoid to topography ratio

The results of the Geoid to Topography Ratio (GTR) analysis carried out over the eleven overlapping blocks of size 3°×2° along the Greater Maldive Ridge are shown in the Table 4. The computations shows that the GTR values over Maldive Ridge and DSC region are limited between the ranges 0.6 – 1.4 m/km for the studied wavelength bands with or without the sediment correction. If one assume a mantle density of 3300 kg/m^3 and seawater density of 1030 kg/m^3, for these GTR range, the corresponding apparent compensation depth ranges from 12.4 km to 28.9 km (Eq. (7)). Scatter plot of two representative blocks (blocks 1 and 8) for the wavelength bands 330 km – 2420 km and 330 km – 800 km are presented in the Fig. 6. It should be noted that an application of isostatic sediment correction introduces negligibly small changes in the GTR values and goodness of fit obtained, while use of different wavelength band shows minor variations in GTR values for the polygonal areas selected.

The spatial variations in GTR obtained for the two wavelength bands analyzed in this study (Fig. 7, middle panel), shows a maximum value of 1.4 m/km in the south, i.e., in the DSC region and decreasing towards north over the Maldive Ridge to a minimum of 0.6 m/km. The correlation between filtered geoid and topography for the northern blocks (Blocks 9, 10 and 11) computed using the 330 km – 2420 km filtered datasets, shows notable decrease in the value of correlation coefficients (Fig. 7a, top panel) compared to the same obtained for southern blocks as wells as using the 330 km – 800 km filtered datasets. This indicates that the wavelength band over which the geoid correlates with topography varies over the northern part. If one examine GTR variations very closely from south to north, it can be seen that, the values are first starting to decrease from the latitude −3° to −1°, i.e., in the DSC region, then attains a constant value up to latitude 2°, and further progressively decreases towards north over the Maldive Ridge.

6. Discussion

6.1. Crustal structure of Maldive Ridge

The crustal model derived from FAG-IOGL data across the Maldive Ridge (Fig. 8) shows that the Moho depth over the Arabian Basin is comparatively shallower (~8.7 km) than the Central Indian Basin (~16 km), east of Maldive Ridge. Similarly, the crust over the Arabian Basin are thinner as compared to that over the Central Indian Basin. The maximum Moho depth value of ~ 26 km are observed beneath the Maldive Ridge. More or less similar Moho depth / crustal thickness variations were also inferred from the three dimensional inversion of mantle residual gravity anomalies over this region (Kunnummal et al., 2018). Interestingly, the deduced crustal model reveals the presence of thin lava flow unit (1–2 km) on either side of the MR probably masking the underlying oceanic crust. This may be a reason for the non-identification of sea-floor spreading anomalies along the ocean floor adjacent to MR. The thickness of the lava flow unit is comparatively larger over the Maldive Ridge inner sea area (~4 km). Towards the east, the lava flows unit is terminated at the Vishnu Fracture Zone. 2D forward modelling along the profile provided a better RMS fit for a density of 2.95 gm/cc for the crust (acoustic basement), which is comparable to the oceanic crustal density. Therefore, it is more likely that the crust underneath the Maldive Ridge part of the Chagos-Laccadive Ridge system is oceanic in nature. However, considering the inherent ambiguities in the forward modelling of gravity data other geophysical, geochemical and finally results from deep drilling are necessary to arrive at a final conclusion on the exact nature of the crust underneath the Maldive Ridge.

6.2. Variations of T_e and GTR over the GMR and tectonic implications

The finer variations in the effective elastic thickness determined along the Greater Maldive Ridge, through 2D and 3D flexural modelling of both the gravity and geoid anomalies revealed a low to moderate T_e values ranging from 6.5–16.5 km. Compared to the T_e values obtained over the DSC region (11–16.5 km), relatively lower T_e values of the order 7–9 km were found over the Maldive Ridge. Previous estimation of T_e using admittance analysis (Ashalatha et al., 1991; Tiwari et al., 2007) and flexural modelling (Watts et al., 2006; Sreejith et al., 2019) also suggested values < 10 km along the Maldive Ridge. However, the slight differences in magnitude of the T_e estimated from present study and previous studies may attributed to the selection of different window size and model parameters adopted for the computation. The T_e variations generally reflects the strength of the lithosphere at the time of the load emplacement and thus it may be used to discriminate between probable genetic processes, chiefly whether the volcanic emplacement was near to an active spreading centre (low T_e) or to off ridge phenomena (high T_e) (Watts, 2001). The global T_e estimates of Watts et al., (2006) assigned seamounts with T_e ranges from 0–12 km to an "on or near ridge" tectonic setting, 12–20 km to "flank ridge" setting and seamounts with T_e > 20 km to an "off ridge" setting. Accordingly, T_e value of 6.5–16.5 km evaluated over the GMR from the present study

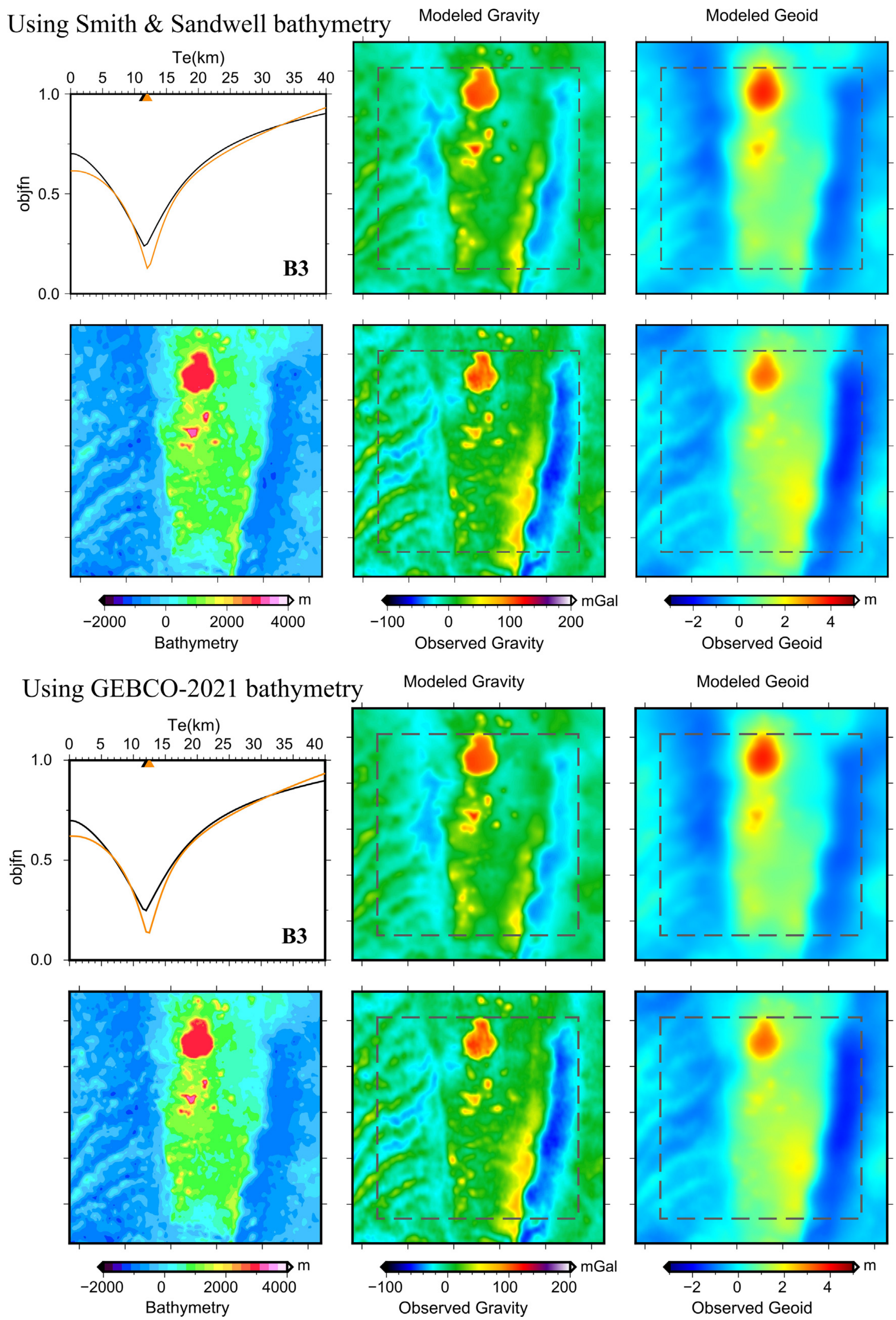

Fig. 5. The observed and predicted gravity/geoid (for best fit T_e) for the blocks B3 (in the DSC region) and B10 (over the Maldive Ridge). The dashed square box represent the region selected for objective function misfit computation. Orange coloured curves corresponds to geoid while black corresponds to FAG-IOGL gravity. The upper and lower half of the figure show the result of 3D flexural modelling using Smith & Sandwell bathymetry and GEBCO-2021 bathymetry respectively. Very long wavelength topography corresponds to spherical harmonics of degree up to 50 are removed from the observed bathymetry.

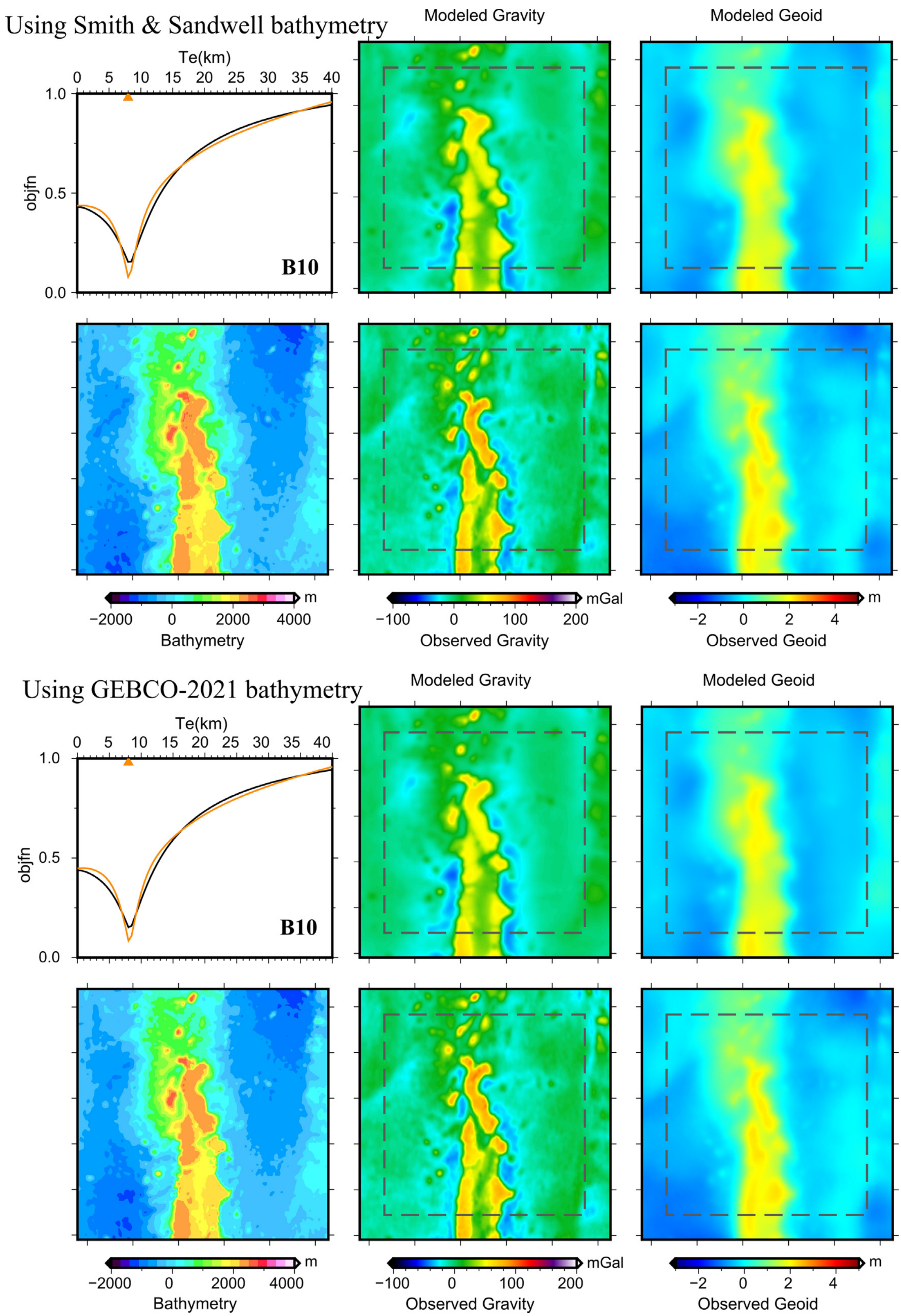

Fig. 5 (*continued*)

suggest a possible emplacement of the ridge near or on the flanks of a spreading centre. Various studies suggests that, Reunion hotpot activity was associated with the formation of Maldive Ridge (Morgan, 1972; Witmarsh, 1974; Duncan and Pyle, 1988). In the context of plume-ridge interaction, a low value of T_e generally indicates the proximity of the plume near to the spreading centre.

Table 4
Results of GTR analysis over several overlapping blocks along the Greater Maldive Ridge. Locations of blocks are shown in Fig. 3c.

Block No.	Centre Latitude (degree)	Using 330 km – 2420 km bandpass filtered geoid and bathymetry						Using 330 km – 800 km bandpass filtered geoid and bathymetry					
		With Sediment Correction (WS)			Without Sediment Correction (WOS)			With Sediment Correction (WS)			Without Sediment Correction (WOS)		
		GTR (m/km)	r	DC (km)	GTR (m/km)	r	DC (km)	GTR (m/km)	r	DC (km)	GTR (m/km)	r	DC (km)
B1	*−3*	1.28 ± 0.16	0.98	26.4	1.27 ± 0.16	0.98	26.3	1.37 ± 0.19	0.99	28.3	1.35 ± 0.18	0.99	27.8
B2	*−2*	1.25 ± 0.14	0.96	25.8	1.24 ± 0.14	0.96	25.5	1.28 ± 0.16	0.98	26.3	1.26 ± 0.15	0.98	25.9
B3	*−1*	1.19 ± 0.12	0.95	24.6	1.18 ± 0.12	0.95	24.2	1.18 ± 0.14	0.97	24.4	1.16 ± 0.13	0.97	23.9
B4	*0*	1.20 ± 0.10	0.97	24.7	1.18 ± 0.10	0.97	24.3	1.10 ± 0.12	0.98	22.6	1.08 ± 0.12	0.99	22.3
B5	*1*	1.20 ± 0.10	0.97	24.8	1.18 ± 0.10	0.98	24.4	1.10 ± 0.13	0.99	21.8	1.04 ± 0.12	0.99	21.4
B6	*2*	1.21 ± 0.10	0.95	24.9	1.19 ± 0.10	0.97	24.6	1.04 ± 0.13	0.97	21.4	1.03 ± 0.13	0.98	21.1
B7	*3*	1.10 ± 0.09	0.92	22.8	1.12 ± 0.09	0.94	23.1	0.96 ± 0.11	0.95	19.8	0.99 ± 0.11	0.97	20.2
B8	*4*	1.01 ± 0.09	0.91	20.7	1.03 ± 0.09	0.94	21.3	0.88 ± 0.11	0.95	18.2	0.91 ± 0.11	0.96	18.8
B9	*5*	0.91 ± 0.10	0.86	18.7	0.95 ± 0.10	0.89	19.7	0.76 ± 0.11	0.93	15.6	0.80 ± 0.11	0.95	16.5
B10	*6*	0.70 ± 0.10	0.77	14.5	0.78 ± 0.11	0.82	16.2	0.64 ± 0.10	0.94	13.3	0.70 ± 0.11	0.95	14.5
B11	*7*	0.58 ± 0.10	0.74	12.0	0.70 ± 0.11	0.81	14.4	0.66 ± 0.09	0.98	13.6	0.74 ± 0.11	0.98	15.3

*r = Correlation Coefficient, DC = Apparent depth of compensation computed using Eq. (7).

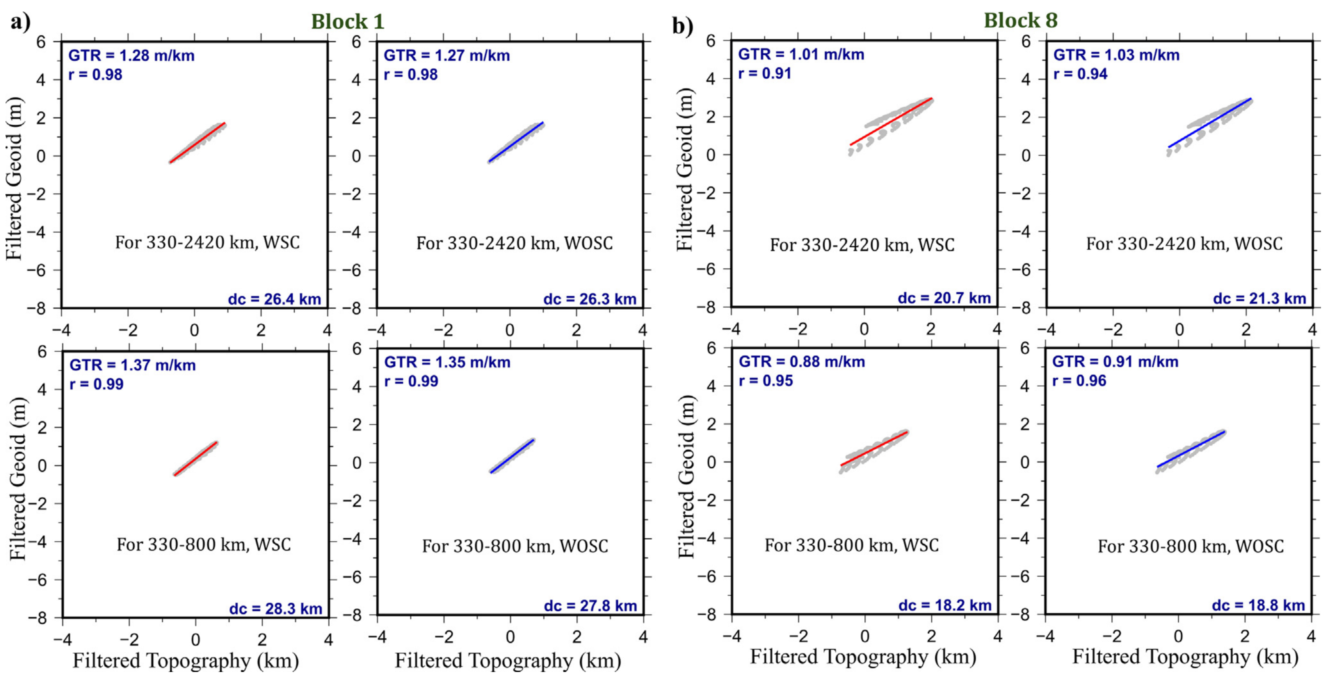

Fig. 6. GTR analysis of two representative blocks, block 1 (a) in the DSC region and block 8, (b) over the MR, carried out for two bandpass filtered geoid and bathymetry. WSC and WOSC represents the GTR analysis carried out with and without removing the isostatic effects of sediments (Sykes, 1996) from the bathymetry respectively. dc = apparent depth of compensation computed from the corresponding GTR value using the Eq. (7).

Therefore, the increasing T_e values from north to south over the GMR indicate that the Reunion plume was close to the spreading centre over the northern side (Maldive Ridge) of the GMR while it was away in the southern side (DSC region). Recent numerical simulation of the Reunion plume interaction with the Central Indian Ridge (Bredow et al., 2017) demonstrated that the Maldive Ridge was formed in the vicinity of the ridge axis, while the DSC region was over a long transform fault. This is borne out in the present study with comparatively low T_e values over the Maldive Ridge and a slightly higher T_e values over the DSC region.

Further, the variations in T_e also depends on temperature, crustal thickness and lithologic variations (Pérez-Gussinyé et al., 2009 and references therein). Thus, the finer variations in T_e can also reflect the variations of the above parameters even if the T_e does not represent an actual depth to the base of the mechanical lithosphere. An examination of the effect of various parameters on the T_e determination using the flexural modelling (Lyons et al, 2000) recommend that, the trend of the elastic thickness estimated along the ridge is usually more effective than its magnitude. That is, even if the magnitude of the T_e changes with the assumption of the parameters used (Table 1), the tectonic implications of spatial variations of T_e can still be considered. All the T_e values evaluated along the axis of the Greater Maldive Ridge from the present study, both using the 2D and 3D flexural modelling are shown in the Fig. 9 along with the various crustal interfaces mapped from our earlier study (Kunnummal and Anand, 2019). The T_e variation from north to south along the GMR shows, in general, a gradually increasing trend with considerable undulations. In the northern part, north of 2° N, the T_e variations are relatively smooth and low (7–9 km) when compared to those in the south of 2° N, where the T_e values are comparatively higher (11 km – 16.5 km), and exhibit significant undulations. Very interestingly, it can be seen that the T_e variations closely and inversely follows the undulations in the Moho depth or the variations in the thickness of the underplated materials. A

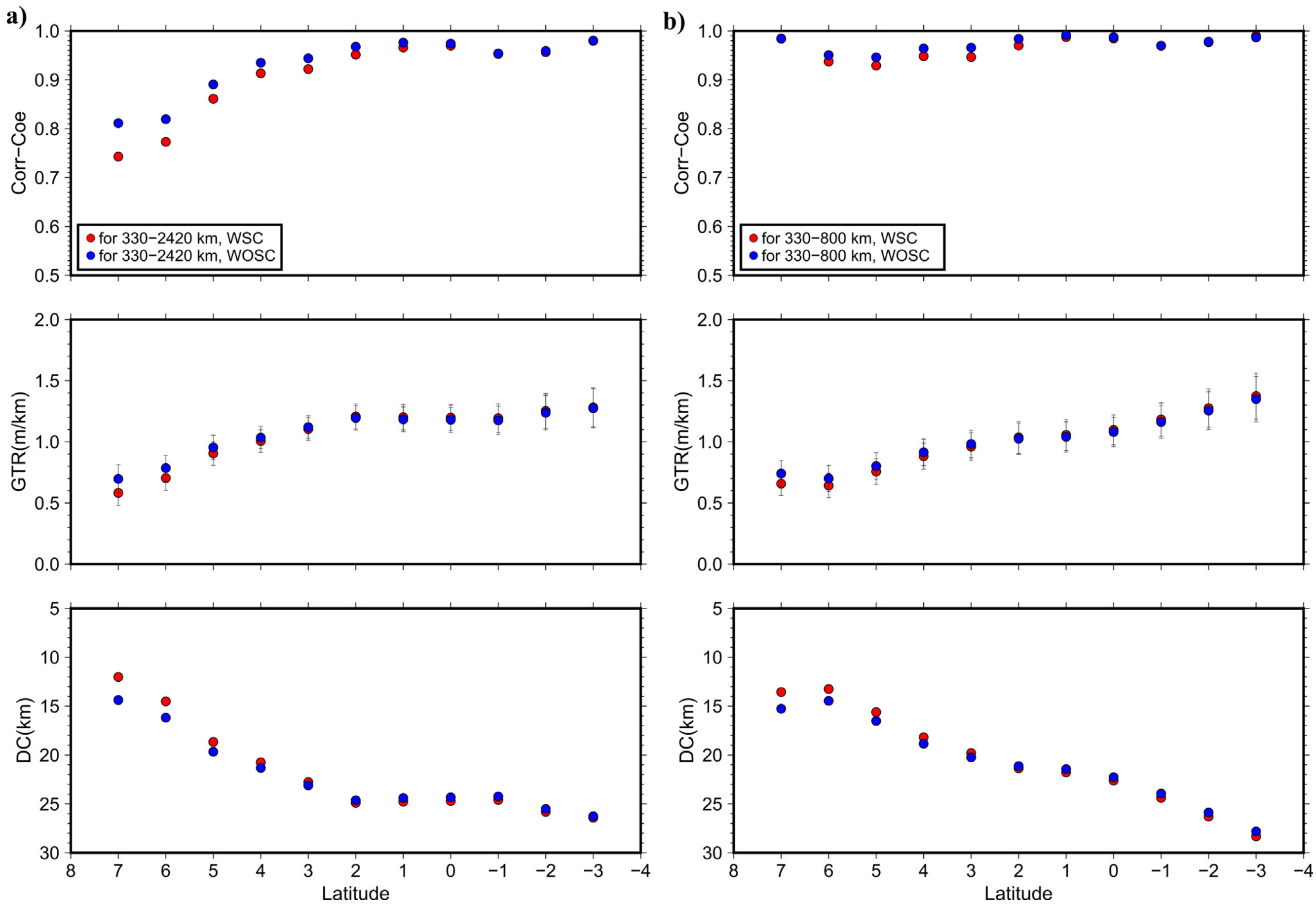

Fig. 7. Results of the GTR analysis carried out using eleven overlapping blocks (B1 to B11, Fig. 3c). Latitude of the centre of each block are used in X direction to mark the GTR values. DC = apparent depth of Compensation, Corr-Coe = Correlation Coefficient. The left (a) and right (b) panel of the Fig. 7, display the results from the analysis of wavelength bands 330 km – 2420 km and 330 km – 800 km respectively, with and without applying isostatic sediment correction.

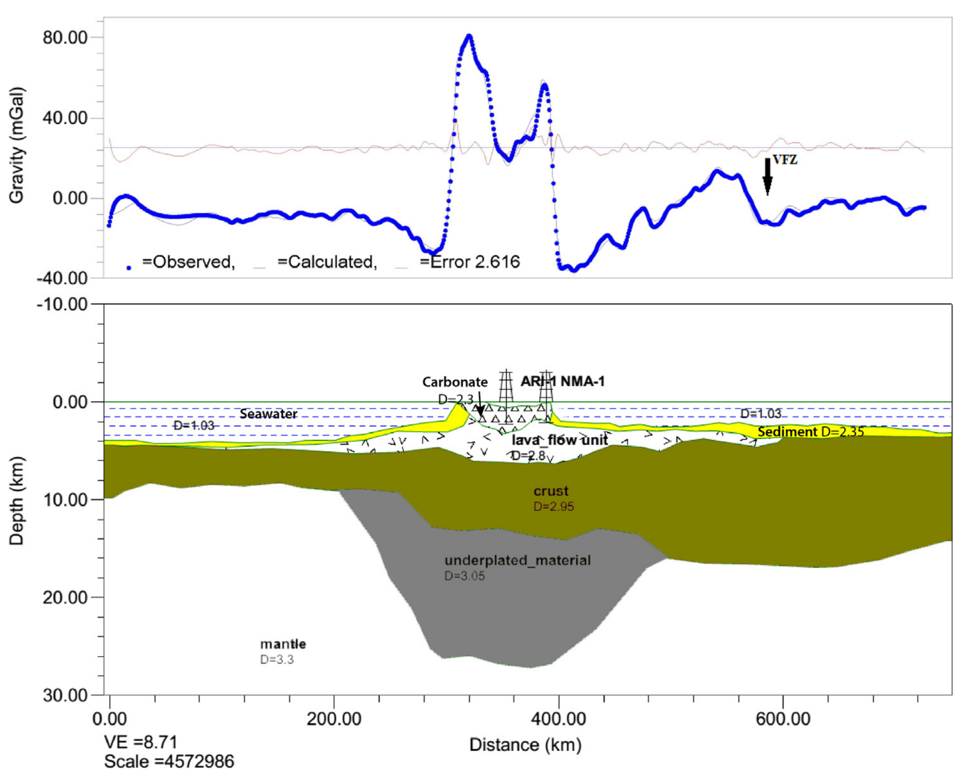

Fig. 8. Two-dimensional crustal model derived from FAG-IOGL data along an E-W profile (CD) over the Maldive Ridge. Refer Fig. 1c for profile location.

higher Moho depth of about 27 km is observed over the Maldive Ridge, while it decreases towards south to a depth of about 15 km in the DSC region (Kunnummal et al., 2018). Similarly, the thickness of the crust over the MR is also higher as compared to the DSC region.

The plume-ridge interaction near to a spreading centre enhances the melt production thereby leading to an increased crustal thickness (Gassmöller et al., 2016). Through simulation of plume-ridge interaction studies, Gassmöller et al. (2016), suggested that the amount of crust generated has an inverse correlation with the distance between plume track and the ridge. That means regions where the plume is very close to the ridge will have much higher crustal thickness compared to regions that are away from the ridge. In addition to the proximity, the time extent of interaction between plume and ridge, i.e., the rate of spreading, also plays an important role in the amount of melt generation. Such a correlation between crustal thickness, variation in melt production, time of interaction and the proximity of the plume and ridge is shown over the Amsterdam-Saint Paul plateau (Maia et al., 2011) and also over the 90°E ridge (Ratheesh-Kumar and Windley, 2013; Sreejith and Krishna, 2015), in the Indian Ocean. Studying the variation of effective elastic thickness and melt production along Deccan-Reunion hotspot, Tiwari et al. (2007) and Suo et al. (2020) suggested an inverse correlation between T_e and melt production rates. As can be seen from Fig. 9, smaller T_e values are observed over regions where the thickness of underplated material, thought to have formed due to the interaction with the hot spot, is more. Combining this information with the estimated T_e values and crustal thickness from our earlier study (Kunnummal et al., 2018), it can be inferred that the Reunion hotspot was very near to the spreading centre of the Central Indian Ridge in the Maldive Ridge segment of the Chagos-Laccadive Ridge. Sreejith et al. (2019) argued that the low T_e observed over the Laccadive part of Chagos-Laccadive Ridge could not be explained by either an on-ridge or off-ridge emplacement on the oceanic lithosphere as the plate tectonic models suggest that the velocity of the Indian plate was exceptionally high commencing from the arrival of Reunion plume at 66 Ma till India-Eurasia collision at 52 Ma. We checked this argument in the GMR part of Chagos-Laccadive Ridge using the age information available from the ODP and industrial wells in the region. The basaltic lava flows recovered from ODP site 714 and 712 (Fig. 1), which are approximately 1000 km apart, respectively provided age of 57 Ma and 49 Ma suggesting a very rapid movement. However the industrial well (NMA1) ~ 90 km southwest of the ODP well 714 provided an age of 55 Ma suggesting that the Indian plate was moving with a moderate speed during this time interval. This suggests that plate movement was variable and the time duration of plate-plume interaction was different from north to south along the GMR. As there is a direct relation between melt generation (crustal thickness) and plume-ridge interaction which will have an inverse relation with T_e, we infer that the plume interacted with the ridge for more time in the northern part of GMR which progressively decreased towards the south. Relatively higher T_e values of 11 km – 16.5 km along with a marked decrease in the crustal thickness (Kunnummal et al., 2018) obtained over the DSC region suggests that this region was formed away from the plume and probably evolved over a transform fault which resisted the magma emplacement with its geometry and lithospheric strength. This inference is in accordance with the studies by Suo et al. (2020) who suggested that the lowest production rate occurred at 50–52 Ma. Fig. 10.e summaries the inference on plume-ridge interaction inferred from the present study. In the presence of underplating (Fontaine et al., 2015) the flexural modelling predicts a slightly higher T_e values (Watts, 2001), therefore the T_e estimates from the present study provides an upper bound to the T_e variations along the Greater Maldive Ridge especially over the Maldive Ridge segment.

The spatial variations in Geoid to Topography Ratio (GTR) over the Greater Maldive Ridge revealed low GTR values ranging from 0.6 – 1.4 m/km. An overall increasing trend of the GTR variations from north to south along the ridge was observed with comparatively low values over the Maldive Ridge (<1 m/km) and slightly higher values over the DSC region (>1 m/km). Similar to the spatial variation in T_e, the trend of the GTR values also changes at 2°N. The variations in the depth of compensation shows a shallow compensation depth (15–23 km) in the northern part (north of 2°N), while the compensation depths gently increases towards south, over the DSC region (>23 km). Studies have established that the low GTR values (0–2 m/km) generally suggests a shallow compensation

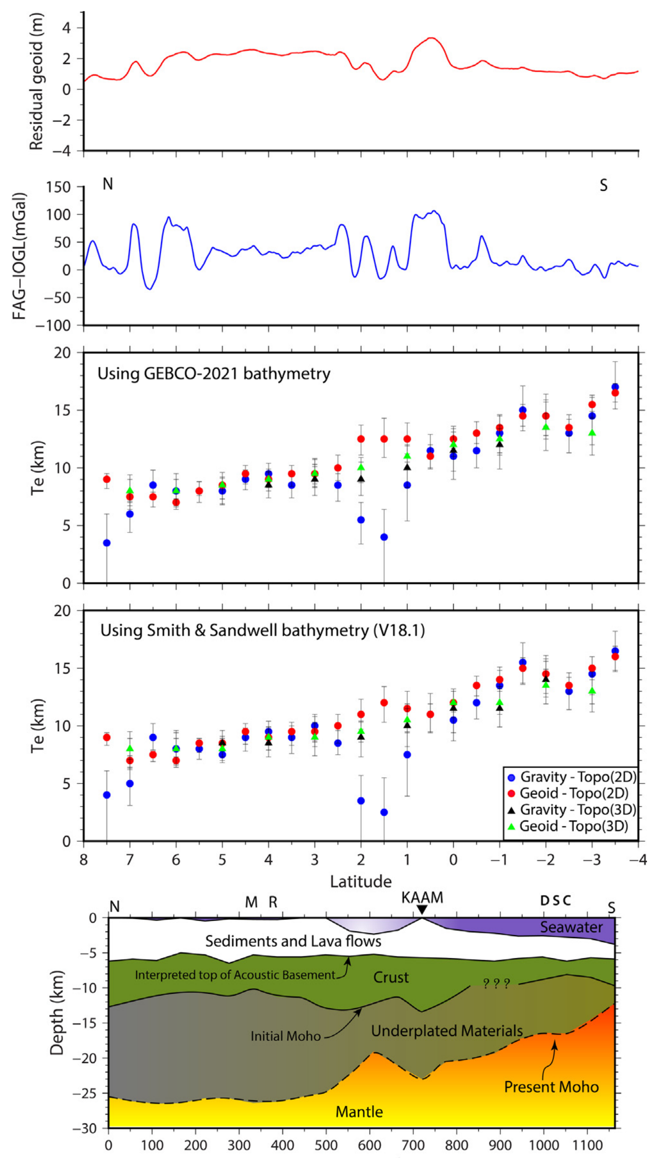

Fig. 9. Spatial variation of T_e values computed from 2D and 3D flexural modelling of FAG-IOGL gravity and residual geoid anomalies along the GMR from north to south (along 73.25° longitude). For comparison, the variations in T_e values obtained both using Smith & Sandwell bathymetry and GEBCO-2021 are shown separately. The error bar represents lower and upper limits of best fit T_e. FAG-IOGL and residual geoid data extracted along a longitudinal transect (along 73.25°) are also depicted. Bottom figure shows the various crustal interfaces mapped from our earlier study (Kunnummal and Anand, 2019) along the same transect.

(e.g., Sandwell and Renkin, 1988). Therefore the low GTR values ranging from 0.6–1.4 m/km obtained from the analysis of several overlapping blocks, predicts a local isostatic compensation mechanism with crustal thickening under the Greater Maldive Ridge. Thus the GTR variation also supports the assumption that the Maldive Ridge was emplaced on a near ridge setting. The Moho depth derived from gravity inversion also suggests a crustal thickening under the GMR (Fig. 10a).

Additionally, a comparison of the global Curie depth with the T_e and GTR variation along the GMR was made in this study to understand, whether, the T_e or GTR predicted along the Greater Maldive Ridge dependent on any temperature perturbations along the ridge. The global Curie-point depth, with a gridding resolution of 10 arc-minute, mapped from the Earth Magnetic Grid (EMAG-2) with 2 arc-minute resolution by Li et al. (2017) over the study region is presented in the supporting information Fig. S5. We are looking at the relative variations of Curie depth over GMR rather than absolute values. One of the main parameter, which controls the Curie depth variation, is the temperature or crustal heat flow with lesser incidence of a petrological boundary (Rajaram et al., 2009). Generally a shallow Curie depth is observed in the region where high heat flow persists. Along the GMR, the Curie depth increases from south to north (as can be seen from Fig. 10b) progressively with age, in accordance with previous observations for world oceans (Li et al., 2017; Gailler et al., 2016). In the study region, over the MR, a slightly deeper Curie depth, (an average of 20 km) was obtained as compared to DSC region, where it averages to 17 km. Occurrence of relatively deeper Curie depth over the MR region, suggests that currently the region is not associated with any thermal anomalies, different from what is observed in the mid-oceanic ridges where there is active magmatism and upwelling of the asthenospheric material (Li et al., 2017). From Fig. 10b, between latitude 2° to 7°N, inferred as on or near axis volcanism, an inverse correlation is observed between excess crustal thickness and Curie depth. Between latitude 4.5° and 5.5°, which we earlier suggested as region where the plume was below the ridge for relatively longer duration with largest excess crustal thickness within MR, the Curie isotherm is shallower suggesting increased temperature. This observation propose that Curie depth in combination with excess crustal thickness can act as a proxy to provide information on the duration of plume-ridge interaction. However, this postulate has to be verified in other tectonic settings as well. In the DSC region where, the plume was interpreted to be over a long transform fault (Fig. 10e), the Curie isotherm is at or below the Moho level. A similar pattern i.e., Curie depth below Moho is observed in the adjacent Arabian Sea as well. Studies conducted on unaltered mantle xenoliths indicate that the uppermost mantle could contain ferromagnetic minerals and it can give rise to long wavelength magnetic anomalies (Ferré et al., 2014). Previous studies (Ildefonse et al., 2010) have also shown that upper part of the lithospheric mantle in older 'oceanic crust' can give rise to magnetic anomalies. This gives additional support to our earlier inference that the DSC region is overlain by oceanic crust (Kunnummal and Anand, 2019). As stated earlier, the plume was over a long transform fault in the DSC region which has hindered melt generation due to which the excess crustal thickness is very less in this region (Fig. 10b). The relatively large T_e and shallower Curie depth in DSC region can be attributed to the presence of transform fault at the time of its formation. This can be due to the fact that although the temperature near transform fault is high, mechanically the lithosphere near transform faults can still retain its strength, as suggested by studies of Lu and Li (2017) in the Arctic region.

Therefore in context of Reunion hotspot interaction with the Central Indian Ridge, the finer variations in T_e, GTR, Moho depth and crustal thickness variations along the Greater Maldive Ridge revealed from the present study, largely support the idea that the Maldive Ridge was emplaced on a near ridge tectonic setting, while the DSC region might have been located over a long transform fault (Fig. 10e). From the present study, it can be seen that GMR, a single

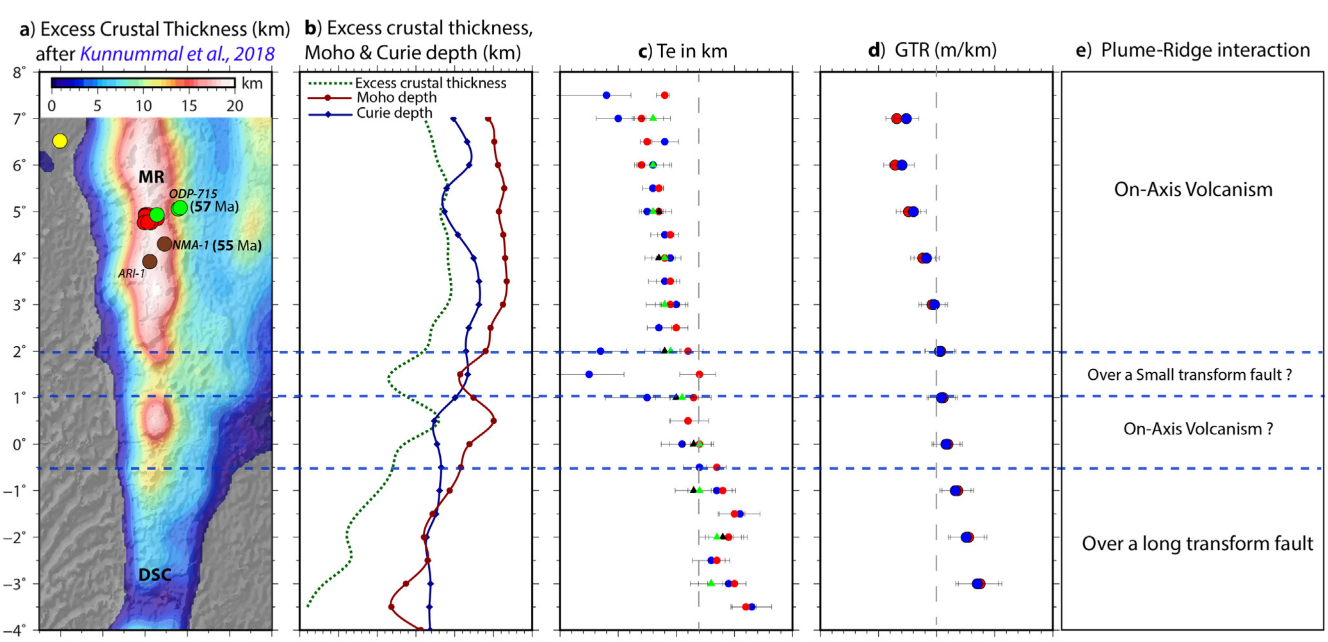

Fig. 10. a) Excess crustal thickness over the GMR obtained after subtracting an average reference crustal thickness of 7 km from the crustal thickness data computed through the 3D inversion of residual mantle gravity anomalies, after Kunnummal et al. (2018). b) Excess crustal thickness, Moho depth (after Kunnummal et al., 2018) and Curie depth (after Li et al., 2017) values extracted along the axis of GR (along 73.25°). c) and d) shows the spatial variations of effective elastic thickness (using Smith & Sandwell bathymetry) and Geoid to Topography Ratio (for the wavelength band 330 km – 800 km) along the axis of GMR respectively. Refer Fig. 7 and Fig. 9 for colour legends. e) Tectonic evolutionary model proposed for the Maldive Ridge and DSC region in context of Reunion hotspot - Central Indian Ridge interaction.

bathymetric feature, is associated with more than one tectonic setting as suggested by Watts et al. (2006). Further detailed investigations along the GMR using multi-channel seismic reflection sections, magnetic and geochemical results from deep drilling, may deliver useful information on nature of the ridge.

7. Conclusions

High resolution satellite derived gravity, geoid and bathymetry over the Greater Maldive Ridge have been analyzed in this study to understand its crustal structure and tectonic evolution. The finer variations in T_e along the GMR are determined from the 2D and 3D flexural modelling employing both the bathymetry-gravity and bathymetry-geoid relationship. The analysis has been performed using two different bathymetric datasets for comparison. The results from the 2D flexural modelling carried out using several median stacked profiles and that from the 3D flexural modelling along several overlapping blocks, shows a similar pattern of T_e variation, both in magnitude and trend along the ridge. The estimated T_e values along the GMR ranges from 6.5 km to 16.5 km with comparatively lower T_e values over the MR (7 km – 9 km) and a slightly higher T_e values over the DSC region (>10 km). The GTR values computed for two wavelength bands show almost similar kind of variation along the ridge with a maximum GTR value of 1.4 m/km in the south, i.e., in the DSC region and decreasing towards north over the Maldive Ridge to a minimum of 0.6 m/km. Integrating the results obtained from the present study with previously published data of crustal thickness, Moho depth and Curie depth along the entire length of the GMR suggest that the Maldive Ridge was formed in the vicinity of spreading centre where as the DSC region was under a long transform fault, and give rise to gap between Chagos Bank and Maldive Ridge during the plume-ridge interaction. The present study also suggests that the Curie isotherm depth in combination with excess crustal thickness can be used as a proxy to throw light on the duration of plume-ridge interaction. Further, detailed paleo-geographic reconstruction studies using high resolution magnetic data along with geochemical data from deep drilling at several locations on the ridge will provide more clues to its tectonic evolution.

CRediT authorship contribution statement

Priyesh Kunnummal: Conceptualization, Methodology, Software, Validation, Visualization, Writing – original draft. **S.P. Anand:** Conceptualization, Methodology, Supervision, Writing – review & editing.

Declaration of Competing Interest

The authors declare that they have no known competing financial interests or personal relationships that could have appeared to influence the work reported in this paper.

Acknowledgements

The authors thank, Prof. D.S. Ramesh, Director of Indian Institute of Geomagnetism for his constant encouragement and support and according permission to publish this work. The authors also thank Prof. Mita Rajaram, for fruitful discussions. We earnestly thank the reviewer Prof. Wenjiao Xiao, three Anonymous reviewers, associate editor Dr. Vasanthi and the Editor for their meticulous reviews and constructive criticisms, which have greatly improved the paper. Funds for carrying out this research at the Indian Institute of Geomagnetism is provided by the Department of Science and Technology (DST), Government of India, New Delhi. Most of the figures were drafted using Generic Mapping Tools (GMT, Wessel and Luis, 2017). The research work presented in this paper is part of the Ph.D. thesis of the first author.

Data Availability Statement

The high resolution satellite derived gravity and bathymetric data sets are available on the Scripps institution of Oceanography (University of California San Diego) website (Gravity: *https://topex.ucsd.edu/WWW_html/mar_grav.html* ; Bathymetry: *https://topex.ucsd.edu/WWW_html/mar_topo.html*). The General Bathymetric Chart of the Oceans (GEBCO, 2021) bathymetry data is available from the website (*https://www.gebco.net/*). The total sediment thickness grid of the world oceans can be downloaded from the NGDC website (*https://ngdc.noaa.gov/mgg/sedthick/*). Computations using the spherical harmonic expansions of geoid (EIGEN-6C4) and topography models are achieved using the calculation services of ICGEM website (*http://icgem.gfz-potsdam.de/calcgrid*). The global mean surface height (DTU15MSS) and mean dynamic topography (DTU15MDT) data sets can be obtained from the DTU Space (Denmark's National Space Institute) ftp site, (*https://ftp.space.dtu.dk/pub/DTU15/1_MIN/*). All other sources used are published and referenced in the manuscript. The MATLAB program codes used in this manuscript are available from the authors upon request (Email: aerospl@yahoo.co.uk and priyeshkunnummal@gmail.com).

Appendix

The importance of inclusion of non-linear terms when modelling the gravity and geoid anomalies due to topographic load and its compensation is demonstrated here using synthetic data and results. Synthetic tests are performed for two topographic loads, case a) Gaussian seamount; case b) line ridge. The first model assumes a Gaussian seamount (Fig. 11a) having a Gaussian height of 3600 m and base radius of 75 km loading an elastic lithosphere of T_e value 6 km. The seamount is placed on flat seafloor of depth 4000 m and the average crustal thickness is taken as 6 km. Similarly, in the second case, a line ridge with a base width of 150 km and height of 3600 m placed in the same environment are considered (Fig. 12a) with similar T_e and crustal thickness values. A line ridge is taken because, most of the aseismic ridges, show considerable elongation and appear to be linear feature rather than a single isolated seamount. The density of seawater, crust and mantle are assumed to be 1030, 2800 and 3400 kg/m^3 respectively (here the density of the topographic load is assumed to be equal to the crustal density). The gravity and geoid response from these two models computed with and without including the nor-linear terms are shown in Fig. 11 (c, f) and Fig. 12 (c, f). The non-linear contributions from the bathymetry and Moho are evaluated up to and including $n = 5$. It can be noted that, from the Fig. 11 and Fig. 12, inclusion of higher order terms have strong effect on the peak amplitude and very less effects on the flanks of the anomaly, in both the case of seamount and line ridge. This shows the significance of consideration of nonlinear terms when attempting to fit the anomaly peaks in the flexural modelling of gravity and geoid anomalies. Further, studies show that the maximum amplitude of the anomaly peak increases as the number of terms in the expansion increases, but converges quickly (e.g., Marks and Smith, 2007). Hence in this paper for flexural modelling, the non-linear contributions from the bathymetry and Moho are evaluated up to and including $n = 5$.

Another important aspect noted in the flexural modelling studies is the effect of assumption of two dimensionality for a three dimensional feature (Ribe, 1982; Filmer et al., 1993; Lyons et al.,

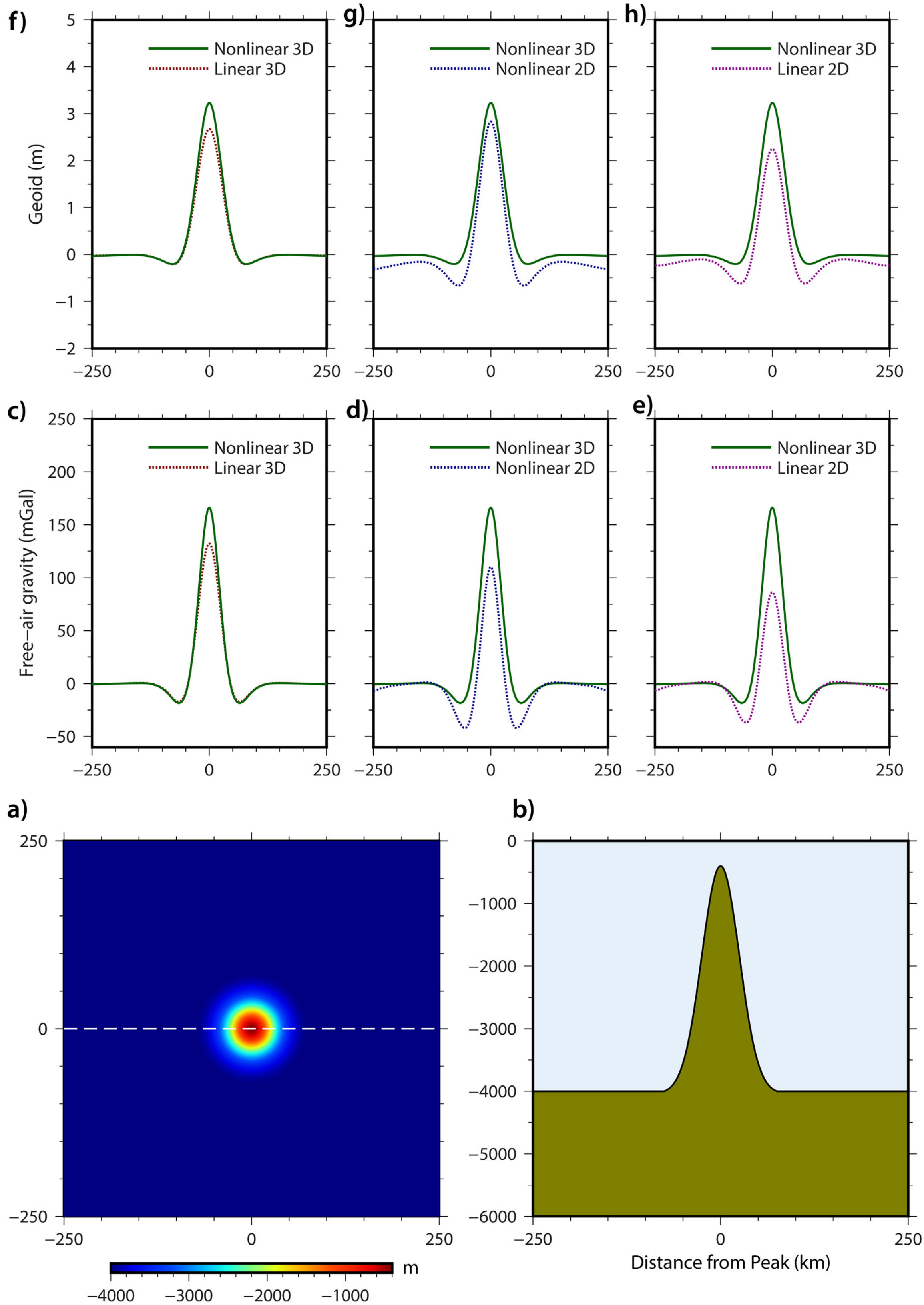

Fig. 11. The effect of dimensionality and the inclusion of higher order terms of bathymetry and Moho topography in the flexural modelling of a seamount is demonstrated here. a) The Gaussian seamount with base radius 75 km and height 3600 m placed on a flat seafloor. b) Represents the bathymetry extracted over a profile shown in Fig. 11a (white dotted line). c) and f) Illustrates the effect of inclusion of higher order terms (n = 5) of bathymetry and Moho. d) , e) and g), h) show the effect of incorrect assumption of two dimensionality in the gravity and geoid anomalies for an isolated seamount. The values of model parameters used areρ_w = 1030 kg/m^3, ρ_c= 2800 kg/m^3, ρ_m= 3400 kg/m^3, d = 6 km, T_e= 6 km.

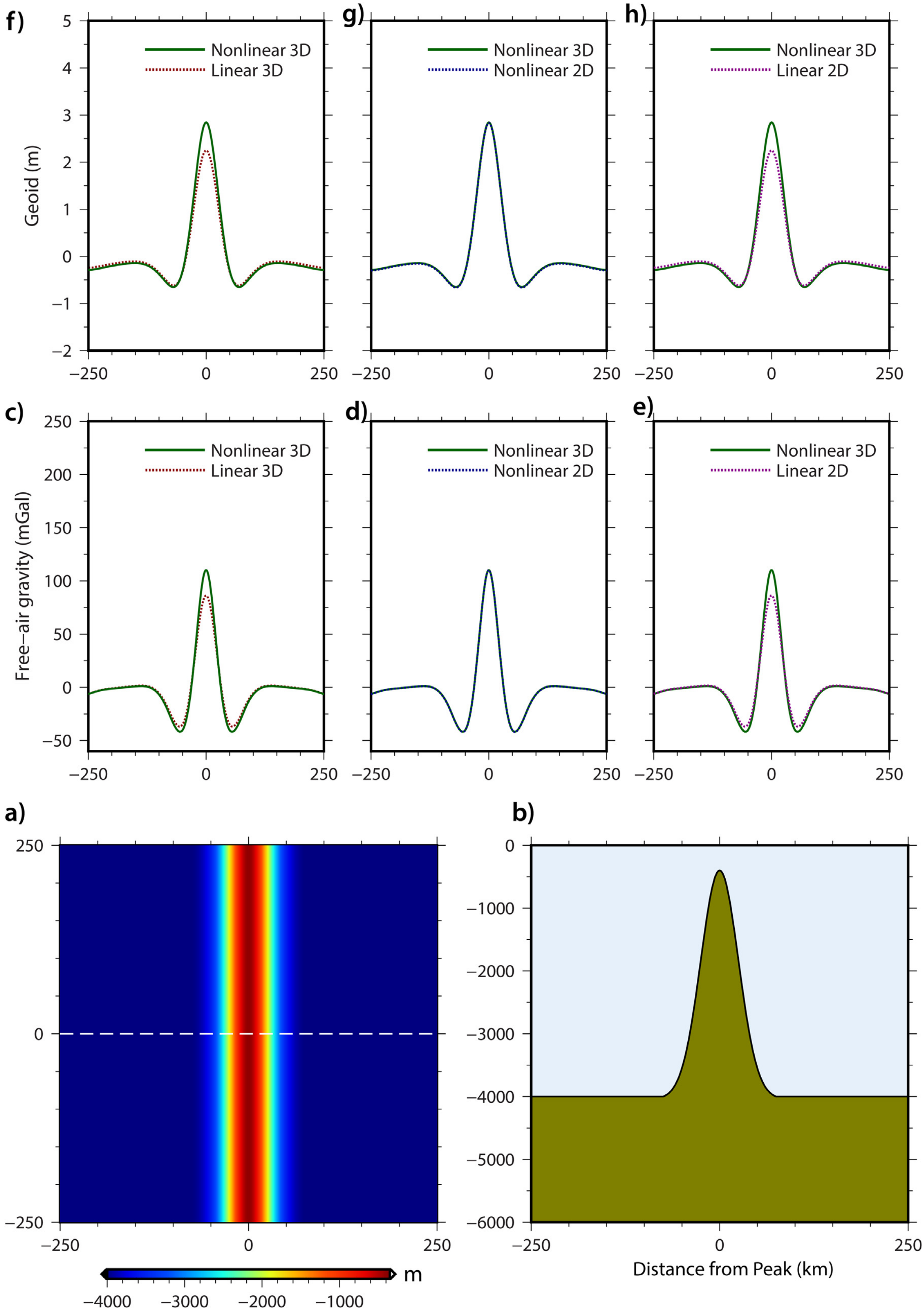

Fig. 12. Model illustrating nonlinear and dimensionality effects in the case of a line ridge. a) A line ridge with base width 150 km and height 3600 m placed on a flat seafloor. b) Represents the bathymetry extracted over a profile shown in Fig. 12a (white dotted line). c) and f) Illustrates the effect of inclusion of higher order terms (n = 5) of bathymetry and Moho. d) , e) and g), h) show the effect of incorrect assumption of two dimensionality in the gravity and geoid anomalies for a line ridge. The values of model parameters used areρ_w = 1030 kg/m^3, ρ_c= 2800 kg/m^3,ρ_m = 3400 kg/m^3, d = 6 km, T_e= 6 km.

2000). Assumption of two dimensionality for a seamount introduces marked effects on the gravity anomalies and have large effect on T_e determination in flexural studies (Lyons et al., 2000). This is demonstrated in the Fig. 11 (d, e and g, h) for the case of seamount. The bathymetry extracted over a profile (Fig. 11.b) from the 3D Gaussian seamount (Fig. 11a) has been assumed as a 2D structure and the model parameters are set same for both 3D and 2D. It appears that the assumption of two dimensionality of seamount causes a false negative side lobes and insufficient peak amplitude, leading to an overestimation in T_e (Lyons et al., 2000). However, in the case of a line ridge, as demonstrated in the Fig. 12 (d, e and g, h) the assumption of two dimensionality as little effect on the gravity and geoid anomalies. Therefore the 2D flexural modelling of gravity and geoid anomalies can also provide reliable T_e estimates if the length of the ridge is much greater than its width and the profile has taken perpendicular to the ridge axis. For the safe assumption of two dimensionality, the length of the ridge should be greater by 250–300 km than the width of the ridge (Ribe, 1982).

Appendix A. Supplementary material

Supplementary data to this article can be found online at https://doi.org/10.1016/j.gr.2022.01.006.

References

Andersen O.B., Knudsen P., Kenyon S., Holmes S., Factor J.K., 2019. Evaluation of the Global Altimetric Marine Gravity Field DTU15: Using Marine Gravity and GOCE Satellite Gravity. In: Freymueller J., Sánchez L. (eds) International Symposium on Advancing Geodesy in a Changing World. International Association of Geodesy Symposia, 149. Springer, Cham. Doi: 10.1007/1345_2018_52

Ashalatha, B., Subrahmanyam, C., Singh, R.N., 1991. Origin and compensation of Chagos-Laccadive Ridge, Indian ocean, from admittance analysis of gravity and bathymetry data. Earth Planet. Sci. Lett. 105 (1-3), 47–54. https://doi.org/10.1016/0012-821X(91)90119-3.

Aubert, O., Droxler, A.W., 1996. Seismic stratigraphy and depositional signatures of the Maldive carbonate system (Indian Ocean). Mar. Petrol. Geo. 13 (5), 503–536. https://doi.org/10.1016/0264-8172(96)00008-6.

Ben Avraham, Z., Bunce, E.T., 1977. Geophysical study of the Chagos-Laccadive Ridge, Indian Ocean. J. Geophys. Res. 82 (8), 1295–1305. https://doi.org/10.1029/JB082i008p01295.

Backman, J., Duncan, R.A., et al., 1988. Proc. ODP, Init. Repts., 115: College Station, TX (Ocean Drilling Program), 589–656. Doi: 10.2973/odp.proc.ir.115.109.1988

Bansal, A.R., Fairhead, J.D., Green, C.M., Fletcher, K.M.U., 2005. Revised gravity for offshore India and the isostatic compensation of submarine features. Tectonophysics 404 (1-2), 1–22. https://doi.org/10.1016/j.tecto.2005.03.017.

Barthelmes, F., Köhler, W., 2016. International Centre for Global Earth Models (ICGEM), in: Drewes, H., Kuglitsch, F., Adám, J. et al., (2016). The Geodesists Handbook 2016, J. Geodesy 90, 907-1205.

Belopolsky, A., Droxler, A., 2003. Imaging Tertiary carbonate system. The Maldives. Indian Ocean. Lead. Edge 22, 646–652. https://doi.org/10.1190/1.1599690.

Betzler, C., Eberli, G.P., Alvarez Zarikian, C.A., Alonso-García, M., Bialik, O.M., Blättler, C.L., et al., 2017. Expedition 359 summary. In Betzler, C., Eberli, G.P., Alvarez Zarikian, C.A., and the Expedition 359 Scientists, Maldives Monsoon and Sea Level. Proceedings of the International Ocean Discovery Program, 359: College Station, TX (International Ocean Discovery Program). Doi: 10.14379/iodp.proc.359.101.2017

Bhattacharya, G.C., Chaubey, A.K., 2001. Western Indian Ocean – a glimpse of the tectonic scenario. In: Sen Gupta, R., Desa, E. (Eds.), The Indian Ocean – A perspective. Oxford-IBH, New Delhi, pp. 691–729.

Bredow, E., Steinberger, B., Gassmöller, R., Dannberg, J., 2017. How plume-ridge interaction shapes the crustal thickness pattern of the Réunion hotspot track. Geochem. Geophys. Geosyst. 18, 2930–2948. https://doi.org/10.1002/2017GC006875.

Cande, S.C., Patriat, P., 2015. The anticorrelated velocities of Africa and India in the Late Cretaceous and early Cenozoic. Geophys. J. Int. 200, 227–243. https://doi.org/10.1093/gji/ggu392.

Cande, S.C., Patriat, P., Dyment, J., 2010. Motion between the Indian, Antarctic and African plates in the early Cenozoic. Geophys. J. Int. 183, 127–149. https://doi.org/10.1111/j.1365-246X.2010.04737.x.

Chand, S., Subrahmanyam, C., 2003. Rifting between India and Madagascar–mechanism and isostasy. Earth Planet. Sci. Lett. 210 (1-2), 317–332. https://doi.org/10.1016/S0012-821X(03)00094-3.

Chapman, M.E., 1979. Techniques for interpretation of geoid anomalies. J. Geophys. Res. 84, 3793–3801. https://doi.org/10.1029/JB084iB08p03793.

Chaubey, A.K., Dyment, J., Bhattacharya, G.C., Royer, J.-Y., Srinivas, K., Yatheesh, V., 2002. Paleogene magnetic isochrons and palaeo-propagators in the Arabian and Eastern Somali basins, NW Indian Ocean. Geolog. Soc. London 195 (1), 71–85. Special Publications.

Chaubey, A.K., Srinivas, K., Ashalatha, B., Rao, D.G., 2008. Isostatic response of the Laccadive Ridge from admittance analysis of gravity and bathymetry data. J. Geodyn. 46 (1-2), 10–20. https://doi.org/10.1016/j.jog.2008.03.001.

Crough, S.T., 1978. Thermal origin of mid-plate hot-spot swells. Geophys. J. Int. 55 (2), 451–469. https://doi.org/10.1111/j.1365-246X.1978.tb04282.x.

Desa, M.A., Ramprasad, T., Kamesh Raju, K.A., 2019. An integrated geophysical study east of the southern Chagos Laccadive Ridge Complex, Central Indian Ocean Basin: Implications for the Rodriguez Triple Junction dynamics in the Late Cretaceous. Mar. Geol. 414, 47–63. https://doi.org/10.1016/j.margeo.2019.05.007.

Dev, S.V., Radhakrishna, M., Subrahmanyam, C., 2007. Estimates of effective elastic thickness along the Southwest continental margin of India using coherence analysis of gravity and bathymetry data - geodynamic implications. Geol. Soc. Ind. 70, 475–487.

Dietz, R.S., Holden, J.C., 1970. Reconstruction of Pangaea: Breakup and dispersion of continents, Permian to Present. J. Geophys. Res. 75 (26), 4939–4956. https://doi.org/10.1029/JB075i026p04939.

Divins, D.L., 2003. Total Sediment Thickness of the World's Oceans & Marginal Seas. NOAA National Geophysical Data Center, Boulder, Colorado, USA.

Dorman, L.M., Lewis, B.T.R., 1970. Experimental isostasy: 1. Theory of the determination of the Earth's isostatic response to a concentrated load. J. Geophys. Res. 75 (17), 3357–3365. https://doi.org/10.1029/JB075i017p03357.

Duncan, R.A., Hargraves, R.B., 1990. In: Proceedings of the Ocean Drilling Program, R. A. Duncan, J. Backman, L. C. Peterson et al., (Eds.), College Station, Texas, Scientific Results. 115, 43-51

Duncan, R.A., Pyle, D.G., 1988. Rapid eruption of the Deccan flood basalts at the Cretaceous/Tertiary boundary. Nature 333 (6176), 841–843. https://doi.org/10.1038/333841a0.

Ferré, E.C., Friedman, S.A., Martín-Hernández, F., Feinberg, J.M., Till, J.L., Ionov, D.A., Conder, J.A., 2014. Eight good reasons why the uppermost mantle could be magnetic. Tectonophysics 624–625, 3–14. https://doi.org/10.1016/j.tecto.2014.01.004.

Filmer, P.E., McNutt, M.K., Wolfe, C.J., 1993. Elastic Thickness of the Lithosphere in the Marquesas and Society Island. J. Geophys. Res. 98, 19565–19577. https://doi.org/10.1029/93JB01720.

Fontaine, F.R., Barruol, G., Tkalčić, H., Wölbern, I., Rümpker, G., Bodin, T., Haugmard, M., 2015. Crustal and uppermost mantle structure variation beneath La Réunion hotspot track. Geophys. J. Int. 203 (1), 107–126. https://doi.org/10.1093/gji/ggv279.

Förste, C., Bruinsma, S., Abrikosov, O., Lemoine, J, M., Marty, J, C., Flechtner, F., Balmino, G., Barthelmes, F., Biancale, R., 2015. EIGEN-6C4, The latest combined global gravity field model including GOCE data up to degree and order 2190 of GFZ Potsdam and GRGS Toulouse. GFZ Data Services. Doi: 10.5880/icgem.2015.1

Francis, T.J.G., Shor, G.G., 1966. Seismic refraction measurements in the northwest Indian Ocean. J. Geophys. Res. 71 (2), 427–449. https://doi.org/10.1029/JZ071i002p00427.

Gailler, L., Lénat, J.F., Blakely, R.J., 2016. Depth to Curie temperature or bottom of the magnetic sources in the volcanic zone of la Réunion hot spot. J. Volcanol. Geotherm. Res. 324, 169–178. https://doi.org/10.1016/j.jvolgeores.2016.06.005.

Gassmöller, R., Dannberg, J., Bredow, E., Steinberger, B., Torsvik, T.H., 2016. Major influence of plume-ridge interaction, lithosphere thickness variations, and global mantle flow on hotspot volcanism-The example of Tristan. Geochem. Geophys. Geosyst. 17 (4), 1454–1479. https://doi.org/10.1002/2015GC006177.

GEBCO Compilation Group, 2021. GEBCO 2021 Grid. Doi: 10.5285/c6612cbe-50b3-0cff-e053-6c86abc09f8f

Geosoft, 2014. Oasis montage data processing and analysis (DPA) systems for Earth Science Applications (ver.8.0). GM-SYS version 7.0 Gravity and magnetic modeling software user guide. Geosoft Inc, Canada

Ghosh, A., Thyagarajulu, G., Steinberger, B., 2017. The importance of upper mantle heterogeneity in generating the Indian Ocean geoid low. Geophys. Res. Lett. 44 (19), 9707–9715. https://doi.org/10.1002/2017GL075392.

Gupta, S., Mishra, S., Rai, S.S., 2010. Magmatic underplating of crust beneath the Laccadive Island, NW Indian Ocean. Geophys. J. Int. 183, 536–542. https://doi.org/10.1111/j.1365-246X.2010.04759.x.

Ildefonse, B. et al., 2010. The MoHole: a Crustal Journey and Mantle Quest, workshop in Kanazawa, Japan, 3–5 June 2010. Sci. Drill. 10, 56–63.

Kahle, H.-G., Chapman, M., Talwani, M., 1978. Detailed 1×1 gravimetric Indian Ocean Geoid and comparison with Geos-3 radar altimeter geoid profiles. Geophys. J. R. Astron. Soc. 55 (3), 703–720. https://doi.org/10.1111/j.1365-246X.1978.tb05938.x.

Kunnummal, P., Anand, S.P., 2019. Qualitative appraisal of high resolution satellite derived free air gravity anomalies over the Maldive Ridge and adjoining ocean basins, western Indian Ocean. J. Asian Earth Sci. 169, 199–209. https://doi.org/10.1016/j.jseaes.2018.08.008.

Kunnummal, P., Anand, S.P., Haritha, C., Rama Rao, P., 2018. Moho depth variations over the Maldive Ridge and adjoining Arabian and Central Indian Basins, Western Indian Ocean, from three dimensional inversion of gravity anomalies. J. Asian Earth Sci. 156, 316–330. https://doi.org/10.1016/j.jseaes.2017.12.012.

Li, C.F., Lu, Y., Wang, J., 2017. A global reference model of Curie-point depths based on EMAG2. Sci. Rep. 7, 45129. https://doi.org/10.1038/srep45129.

Lu, Y., Li, C.F., 2017. Comprehensive analysis of Curie-point depths and lithospheric effective elastic thickness at Arctic Region. American Geophysical Union, Fall Meeting 2017, abstract #T13B-0526. Bibcode: 2017AGUFM.T13B0526L

Luis, J.F., Neves, M.C., 2006. The isostatic compensation of the Azores Plateau: A 3D admittance and coherence analysis. J. Volcanol. Geotherm. Res. 156 (1-2), 10–22. https://doi.org/10.1016/j.jvolgeores.2006.03.010.
Lyons, S.N., Sandwell, D.T., Smith, W.H.F., 2000. Three-dimensional estimation of elastic thickness under the Louisville Ridge. J. Geophys. Res. Solid Earth 105 (B6), 13239–13252. https://doi.org/10.1029/2000JB900065.
Maia, M., Pessanha, I., Courrèges, E., Patriat, M., Gente, P., Hémond, C., Janin, M., Johnson, K., Roest, W., Royer, J.-Y., Vatteville, J., 2011. Building of the Amsterdam-Saint Paul plateau: A 10 Myr history of a ridge-hot spot interaction and variations in the strength of the hot spot source. J. Geophys. Res. 116, B09104. https://doi.org/10.1029/2010JB007768.
Marks, K.M., Smith, W.H.F., 2007. Some remarks on resolving seamounts in satellite gravity. Geophys. Res. Lett. 34, 1–4. https://doi.org/10.1029/2006GL028857.
McKenzie, D., Sclater, J.G., 1971. The evolution of the Indian Ocean since the Late Cretaceous. Geophys. J. Int. 24, 437–528. https://doi.org/10.1111/j.1365-246X.1971.tb02190.x.
McKenzie, D., Watts, A., Parsons, B., Roufosse, M., 1980. Planform of mantle convection beneath the Pacific Ocean. Nature 288 (5790), 442–446. https://doi.org/10.1038/288442a0.
Mishra, A., Chaubey, A.K., Sreejith, K.M., Kumar, S., 2018. Crustal underplating and effective elastic plate thickness of the Laxmi Ridge, northern Arabian Sea. Tectonophysics 744, 82–92. https://doi.org/10.1016/j.tecto.2018.06.013.
Mishra, A., Chaubey, A.K., Kumar, S., Kumar, P.V., Kumar, P., Dubey, K.M., 2020. Does the Laxmi Ridge continue towards the Laccadive Ridge? New insights from an integrated geophysical study. J. Asian Earth Sci. 201, 104491. https://doi.org/10.1016/j.jseaes.2020.104491.
Monnereau, M., Cazenave, A., 1988. Variation of the apparent compensation depth of hotspot swells with age of plate. Earth Planet. Sci. Lett. 91 (1-2), 179–197. https://doi.org/10.1016/0012-821X(88)90160-4.
Morgan, W.J., 1972. Deep Mantle Convection Plumes and Plate Motions. Am. Assoc. Pet. Geol. Bull. 56, 203–213. https://doi.org/10.1306/819A3E50-16C5-11D7-8645000102C1865D.
Morgan, W.J., 1981. In: The Sea (Vol. 7): The Oceanic Lithosphere, C. Emiliani (Ed.), Wiley-Interscience, NewYork, 443-487
Parker, R.L., 1973. The rapid calculation of potential anomalies. Geophys. J. R. Astron. Soc. 31 (4), 447–455. https://doi.org/10.1111/j.1365-246X.1973.tb06513.x.
Paul, J., Singh, R.N., 1992. Modelling of the gravity effects of flexurally compensating thin layers under the Afanasy-Nikitin seamount. Tectonophysics 206 (3-4), 365–369. https://doi.org/10.1016/0040-1951(92)90387-L.
Pérez-Gussinyé, M., Metois, M., Fernández, M., Vergés, J., Fullea, J., Lowry, A.R., 2009. Effective elastic thickness of Africa and its relationship to other proxies for lithospheric structure and surface tectonics. Earth Planet. Sci. Lett. 287 (1-2), 152–167. https://doi.org/10.1016/j.epsl.2009.08.004.
Krishna, M.R., 1996. Isostatic response of the Central Indian Ridge (western Indian Ocean) based on transfer function analysis of gravity and bathymetry data. Tectonophysics 257 (2-4), 137–148. https://doi.org/10.1016/0040-1951(95)00114-X.
Rajaram, M., Anand, S.P., Hemant, K., Purucker, M.E., 2009. Curie isotherm map of Indian subcontinent from satellite and aeromagnetic data. Earth Planet. Sci. Lett. 281 (3-4), 147–158. https://doi.org/10.1016/j.epsl.2009.02.013.
Rajesh, S., Majumdar, T.J., 2009. Geoid height versus topography of the Northern Ninetyeast Ridge: implications on crustal compensation. Mar. Geophys. Res. 30 (4), 251–264. https://doi.org/10.1007/s11001-010-9088-7.
Rao, G.S., Radhakrishna, M., Sreejith, K.M., Krishna, K.S., Bull, J.M., 2016. Lithosphere structure and upper mantle characteristics below the Bay of Bengal. Geophys. J. Int. 206 (1), 675–695. https://doi.org/10.1093/gji/ggw162.
Ratheesh-Kumar, R.T., Ishwar-Kumar, C., Windley, B.F., Razakamanana, T., Nair, R.R., Sajeev, K., 2015. India-Madagascar paleo-fit based on flexural isostasy of their rifted margins. Gondwana Res. 28 (2), 581–600. https://doi.org/10.1016/j.gr.2014.06.008.
Ratheesh-Kumar, R.T., Windley, B.F., 2013. Spatial variations of effective elastic thickness over the Ninetyeast Ridge and implications for its structure and tectonic evolution. Tectonophysics 608, 847–856. https://doi.org/10.1016/j.tecto.2013.07.034.
Ratheesh-Kumar, R.T., Xiao, W., 2018. Effective elastic thickness along the conjugate passive margins of India, Madagascar and Antarctica: A re-evaluation using the Hermite multitaper Bouguer coherence application. J. Asian Earth Sci. 157, 40–56. https://doi.org/10.1016/j.jseaes.2017.03.019.
Ribe, N.M., 1982. On the interpretation of frequency response functions for oceanic gravity and bathymetry. Geophys. J. R. Astron. Soc. 70 (2), 273–294. https://doi.org/10.1111/j.1365-246X.1982.tb04968.x.
Sandwell, D.T., MacKenzie, K.R., 1989. Geoid height versus topography for oceanic plateaus and swells. J. Geophys. Res. Solid Earth 94, 7403–7418. https://doi.org/10.1029/JB094iB06p07403.
Sandwell, D.T., Müller, R.D., Smith, W.H.F., Garcia, E., Francis, R., 2014. New global marine gravity model from CryoSat-2 and Jason-1 reveals buried tectonic structure. Science 346 (6205), 65–67.
Sandwell, D.T., Renkin, M.L., 1988. Compensation of swells and plateaus in the North Pacific: No direct evidence for mantle convection. J. Geophys. Res. Solid Earth 93, 2775–2783. https://doi.org/10.1029/JB093iB04p02775.
Sandwell, D.T., Smith, W.H.F., 2009. Global marine gravity from retracked Geosat and ERS-1 altimetry: Ridge segmentation versus spreading rate. J. Geophys. Res. 114, B01411. https://doi.org/10.1029/2008JB006008.
Smith, W.H.F., Sandwell, D.T., 1997. Global Sea Floor Topography from Satellite Altimetry and Ship Depth Soundings. Science 277 (5334), 1956–1962.
Smith, W.H.F., Staudigel, H., Watts, A.B., Pringle, M.S., 1989. The Magellan Seamounts: Early Cretaceous record of the South Pacific isotopic and thermal anomaly. J. Geophys. Res. Solid Earth 94 (B8), 10501–10523. https://doi.org/10.1029/JB094iB08p10501.
Sreejith, K.M., Krishna, K.S., 2013. Spatial variations in isostatic compensation mechanisms of the Ninetyeast Ridge and their tectonic significance. J. Geophys. Res. Solid Earth 118 (10), 5165–5184. https://doi.org/10.1002/jgrb.50383.
Sreejith, K.M., Krishna, K.S., 2015. Magma production rate along the Ninetyeast Ridge and its relationship to Indian plate motion and Kerguelen hot spot activity. Geophys. Res. Lett. 42 (4), 1105–1112. https://doi.org/10.1002/2014GL062993.
Sreejith, K.M., Rajesh, S., Majumdar, T.J., Rao, G.S., Radhakrishna, M., Krishna, K.S., Rajawat, A.S., 2013. High-resolution residual geoid and gravity anomaly data of the northern Indian Ocean – an input to geological understanding. J. Asian Earth Sci. 62, 616–626. https://doi.org/10.1016/j.jseaes.2012.11.010.
Sreejith, K.M., Unnikrishnan, P., Radhakrishna, M., 2019. Isostasy and crustal structure of the Chagos-Laccadive Ridge, Western Indian Ocean: Geodynamic implications. J. Earth Syst. Sci. 128, 157. https://doi.org/10.1007/s12040-019-1161-2.
Suo, Y., Li, S., Cao, X., Dong, H., Li, X., Wang, X., 2020. Two-stage eastward diachronous model of India-Eurasia collision: Constraints from the intraplate tectonic records in Northeast Indian Ocean. Gondwana Res. https://doi.org/10.1016/j.gr.2020.01.006.
Sykes, T.J.S., 1996. A correction for sediment load upon the ocean floor: uniform versus varying sediment density estimations-implications isostatic correction. Mar. Geol. 133, 35–49. https://doi.org/10.1016/0025-3227(96)00016-3.
Talwani, M., Worzel, J.L., Landisman, M., 1959. Rapid gravity computations for two dimensional bodies with application to the Mendocino submarine fracture zone. J. Geophys. Res. 64 (1), 49–59. https://doi.org/10.1029/JZ064i001p00049.
Tiwari, V.M., Grevemeyer, I., Singh, B., Phipps Morgan, J., 2007. Variation of effective elastic thickness and melt production along the Deccan-Reunion hotspot track. Earth Planet. Sci. Lett. 264 (1-2), 9–21. https://doi.org/10.1016/j.epsl.2007.08.023.
Torsvik, T.H., Amundsen, H., Hartz, E.H., Corfu, F., Kusznir, N., Gaina, C., Doubrovine, P.V., Steinberger, B., Ashwal, L.D., Jamtveit, B., 2013. A Precambrian microcontinent in the Indian Ocean. Nat. Geosci. 6 (3), 223–227. https://doi.org/10.1038/ngeo1736.
Trivedi, D., Maji, T.K., Sengupta, D., Nair, R.R., 2012. Reappraisal of effective elastic thickness in the South-West Indian Ocean, and its possible implications. Ann. Geophys. 55, 265–272. https://doi.org/10.4401/ag-5171.
Watts, A.B., 2001. Isostasy and Flexure of the Lithosphere. Cambridge University Press.
Watts, A.B., Sandwell, D.T., Smith, W.H.F., Wessel, P., 2006. Global gravity, bathymetry, and the distribution of submarine volcanism through space and time. J. Geophys. Res. Solid Earth 111, 1–26. https://doi.org/10.1029/2005JB004083.
Wessel, P., Luis, J.F., 2017. The GMT/MATLAB Toolbox. Geochem. Geophys. Geosyst. 18 (2), 811–823. https://doi.org/10.1002/2016GC006723.
Whitmarsh, R.B., 1974. Some aspects of plate tectonics in the Arabian Sea, in: Initial Reports of the Deep Sea Drilling Project, 23, US Govt. Printing Office, Washington. 527-535. Doi: 10.2973/dsdp.proc.23.114.1974
Whittaker, J.M., Goncharov, A., Williams, S.E., Müller, R.D., Leitchenkov, G., 2013. Global sediment thickness data set updated for the Australian-Antarctic Southern Ocean. Geochem. Geophys. Geosyst. 14 (8), 3297–3305. https://doi.org/10.1002/ggge.20181.
Won, I.J., Bevis, M., 1987. Computing the gravitational and magnetic anomalies due to a polygon: Algorithms and FORTRAN subroutines. Geophys. 52 (2), 232–238. https://doi.org/10.1190/1.1442298.
Yatheesh, V., Dyment, J., Bhattacharya, G.C., Royer, J.Y., Kamesh Raju, K.A., Ramprasad, T., Chaubey, A.K., Patriat, P., Srinivas, K., Choi, Y., 2019. Detailed structure and plate reconstructions of the Central Indian Ocean between 83.0 and 42.5 Ma (Chrons 34 and 20). J. Geophys. Res. Solid Earth 124 (5), 4305–4322. https://doi.org/10.1029/2018JB016812.